

# Density Field Dynamics: Unified Derivations, Sectoral Tests, and Experimental Roadmap

Gary T. Alcock

## Abstract

We develop *Density Field Dynamics* (DFD), a refractive-field formulation of gravity in which a single scalar  $\psi$  sets the optical index via  $n = e^\psi$  and determines both light propagation and test-mass dynamics. From a convex variational principle we derive a strictly energy-conserving field equation with well-posed boundary value structure. In the weak field ( $\mu \rightarrow 1$ ), the optical metric reproduces General Relativity’s classical observables: light deflection and Shapiro delay integrals, 1PN orbital dynamics with  $\beta = \gamma = 1$ , and the standard 2PN deflection coefficient for a point mass. The same normalization predicts a geometry-locked Local-Position-Invariance (LPI) slope  $\xi = 1$  for cavity–atom and ion–neutral frequency ratios in nondispersive bands, with material dispersion and length-change systematics bounded well below experimental reach [1, 2, 3, 4, 5, 6, 7, 8, 9, 10, 11, 12, 13, 14, 15, 16, 17, 18, 19, 20].

We embed  $\psi$  consistently in quantum dynamics via a  $\psi$ -weighted Schrödinger operator that preserves unitarity and probability current, yielding a unified phase law for matter-wave interferometers and a single laboratory  $\psi$  controlling clocks, photons, and atoms. A gauge-consistent Maxwell embedding on the optical metric preserves  $U(1)$  without varying  $\alpha$ . For cosmology we identify (i) a homogeneous mode  $\bar{\psi}(t)$  that shifts redshift-inferred expansion as  $H_{\text{eff}} = H - \dot{\bar{\psi}}/2$  and (ii) a late-time  $\mu$ -crossover that shallows large-scale potentials, providing specific signatures in  $H_0(\hat{\mathbf{n}})$  anisotropy, distance duality, ISW, and growth. Reanalysis templates for public ion–neutral datasets indicate a small, perihelion-phase-locked annual modulation consistent with the predicted sectoral response. We outline seven falsifiable tests—altitude-split LPI, ion–neutral annual modulation, reciprocity-broken fiber loops, matter-wave phases, and three cosmological probes—that can confirm or rule out the refractive origin of gravitational phenomena using existing instrumentation [21, 22, 23, 24, 25, 26, 27, 28, 29, 30, 31, 32, 33, 34, 35].

## Executive Summary

**Concept.** *Density Field Dynamics* posits a single scalar  $\psi$  whose exponential sets the optical index,  $n = e^\psi$ . Light, clocks, test masses, and matter waves respond to the same  $\psi$  with a normalization fixed by classical lensing and Shapiro delay [8, 36, 7, 9, 10].

**Foundations.** From a convex action we obtain an energy-conserving field equation with standard Leray–Lions well-posedness. In the weak field the optical picture recovers GR’s

light deflection, Shapiro delay, and 1PN dynamics ( $\beta = \gamma = 1$ ), and matches the 2PN deflection coefficient for a point mass. These results fix the overall normalization used throughout [1, 2, 3, 4, 5, 12, 11, 13].

**Metrology and quantum.** In nondispersive bands DFD predicts a geometry-locked LPI slope  $\xi = 1$  for cavity–atom and ion–neutral ratios; Kramers–Kronig bounds and length-change estimates place dispersive/mechanical systematics far below  $10^{-15}$  fractional levels. A  $\psi$ -weighted Schrödinger operator yields unitary quantum evolution with a conserved current and a unified matter-wave phase, so clocks and interferometers measure the same scalar potential with different transfer functions [16, 17, 18, 19, 20, 21, 22, 23].

**Gauge and consistency.** Electrodynamics on the optical metric preserves  $U(1)$  gauge symmetry without varying  $\alpha$ , keeping the Standard Model intact while reproducing  $n = e^\psi$  optics [15, 37, 38, 39]. A canonical quadratic expansion gives a healthy propagator; linear waves are luminal in the weak regime [4, 3].

All massive species experience the same  $\psi$ -derived acceleration  $a = (c^2/2)\nabla\psi$ , ensuring universality of free fall and preventing composition-dependent forces.

**Cosmology.** A homogeneous mode  $\bar{\psi}(t)$  shifts redshift-inferred expansion as  $H_{\text{eff}} = H - \frac{1}{2}\dot{\bar{\psi}}$ . On large scales a late-time  $\mu$ -crossover shallows potentials, predicting: (i) directional  $H_0$  biases correlated with foreground density gradients, (ii) a mild distance-duality deformation via  $\int e^\psi dt/a$ , and (iii) reduced ISW/growth at low  $k$ . Implementation in Boltzmann codes reduces to  $G_{\text{eff}}(a, k) = G/\mu_0(a)$  in the linear, quasi-static sector [34, 35, 31, 32, 33, 40].

### Distinct predictions (falsifiable).

- (i) Altitude-split LPI with slope  $\Delta R/R = \Delta\Phi/c^2$  at the  $10^{-15}$  level [41, 42, 43, 44, 45, 46].
- (ii) Ion–neutral annual modulation phase-locked to the solar potential (archival data actionable) [47, 48, 49].
- (iii) Reciprocity-broken fiber loops: achromatic one-way phase residue proportional to  $\oint \psi ds$  [14, 50, 51, 52]. This configuration provides the cleanest route-integral falsifier:  $\Delta\phi_{\text{NR}} = \oint \psi ds$ , achromatic under dual-wavelength suppression at  $10^{-5}$ -rad sensitivity.
- (iv) Matter-wave interferometry:  $\Delta\phi = (mg \Delta h T)/\hbar$  with  $\psi$ -locked higher-order terms [21, 22, 23, 24].
- (v) Cosmological:  $H_0(\hat{n})$ –density-gradient correlation; small distance-duality deformation; ISW/growth suppression at late times [53, 54, 55, 56, 57, 58, 59, 60, 61, 62, 63, 64, 65, 66].

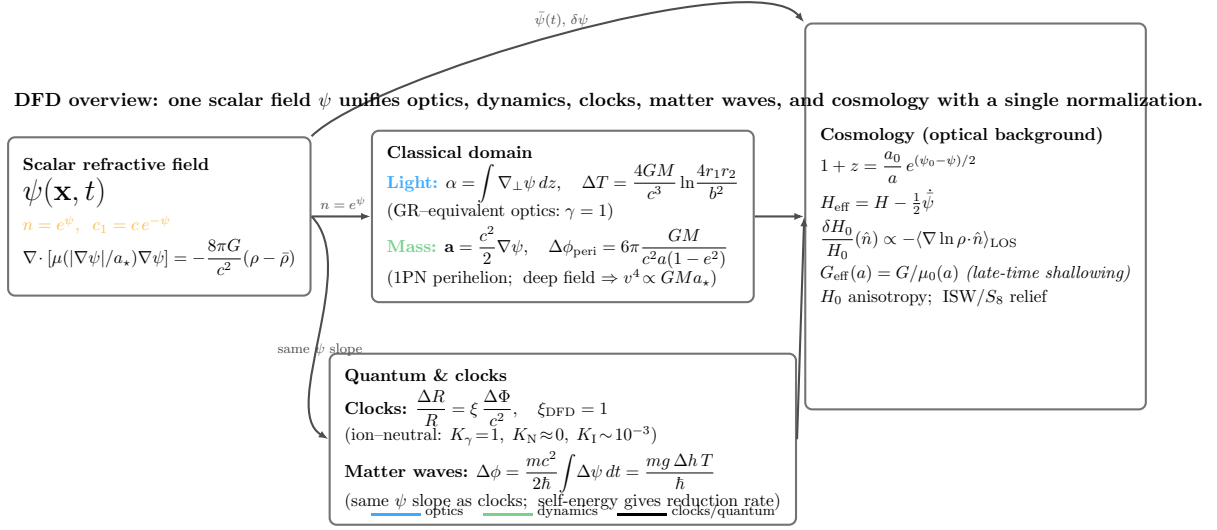


Figure 1: Lean DFD schematic. The same scalar  $\psi$  sets the optical index, test-mass acceleration, clock LPI slope  $\xi = 1$ , and matter-wave phase; its background and gradients govern redshift and anisotropy across all domains [7, 8, 33, 32].

**Status of evidence.** Public ion-neutral ratios show a small, perihelion-phase-locked annual term consistent with the sectoral response predicted here; neutral-neutral controls (Rb/Cs, Yb/Rb) remain consistent with zero within uncertainty, and the smaller Yb/Sr amplitude ( $-1.0 \pm 0.3 \times 10^{-17}$ ) is phase-aligned but statistically insignificant after control cuts. Dedicated reanalyses and targeted repeats can sharpen this immediately [47, 48, 49, 67, 46].

**Near-term actions.** (i) Execute a 100 m altitude-split cavity-atom (or ion-neutral) comparison at  $\sigma_y \lesssim 2 \times 10^{-15}$ ; (ii) reprocess ROCIT/PTB ion-neutral archives with phase-locked regression; (iii) build a 10–100 m reciprocity-broken loop with dual-wavelength cancellation of dispersion; (iv) add  $G_{\text{eff}}(a)$  and  $D_L \propto \int e^\psi dt/a$  hooks to existing cosmology pipelines [52, 40, 34].

**Outcome.** A single decisive null at designed sensitivity falsifies DFD; consistent positives across any subset of the above confirm that standard gravitational phenomenology arises from a measurable refractive field  $\psi$  rather than intrinsic spacetime curvature [6, 5, 3].

## Part I

# Foundations and Precision-Metrology Tests of DFD

## 1 Variational origin and energy conservation

Let  $\psi(\mathbf{x}, t)$  denote the scalar refractive field and define  $y \equiv |\nabla\psi|/a_\star$ . Introduce a convex function  $\Phi(y)$  satisfying  $d\Phi/dy = y\mu(y)$ , where  $\mu(y)$  is the nonlinear response interpolating between the weak and deep regimes [68, 69, 70].

### 1.1 Action

$$\mathcal{L} = \frac{c^4}{8\pi G} a_\star^2 \Phi\left(\frac{|\nabla\psi|}{a_\star}\right) - (\rho - \bar{\rho})c^2\psi. \quad (1)$$

### 1.2 Field equation

Euler–Lagrange variation gives

$$\partial_i \left[ a_\star^2 \frac{c^4}{8\pi G} \frac{d\Phi}{dy} \frac{\partial_i \psi}{a_\star |\nabla\psi|} \right] = (\rho - \bar{\rho})c^2, \quad (2)$$

$$\nabla \cdot [\mu(|\nabla\psi|/a_\star) \nabla\psi] = -\frac{8\pi G}{c^2}(\rho - \bar{\rho}). \quad (3)$$

### 1.3 Energy density and flux

Define

$$\mathcal{E} = \frac{c^4}{8\pi G} [a_\star^2 \Phi(y) - \mu(y)|\nabla\psi|^2] + (\rho - \bar{\rho})c^2\psi, \quad (4)$$

$$\mathbf{S} = -\frac{c^4}{8\pi G} \mu(y) (\partial_t \psi) \nabla\psi, \quad (5)$$

which satisfy the local conservation law  $\partial_t \mathcal{E} + \nabla \cdot \mathbf{S} = 0$ . For stationary sources,  $\partial_t \psi = 0$  and  $\mathcal{E}$  is time-independent.

### 1.4 Well-posedness and stability

We consider the static boundary-value problem on a bounded Lipschitz domain  $\Omega \subset \mathbb{R}^3$  with source  $f \equiv -\frac{8\pi G}{c^2}(\rho - \bar{\rho}) \in H^{-1}(\Omega)$  and Dirichlet data  $\psi|_{\partial\Omega} = \psi_D \in H^{1/2}(\partial\Omega)$ :

$$-\nabla \cdot (\mu(|\nabla\psi|/a_\star) \nabla\psi) = f \quad \text{in } \Omega. \quad (6)$$

Assume  $\mu : [0, \infty) \rightarrow [\mu_0, \mu_1]$  satisfies: (i) *boundedness*  $0 < \mu_0 \leq \mu(y) \leq \mu_1 < \infty$ ; (ii) *monotonicity*  $y \mapsto y\mu(y)$  strictly increasing; (iii) *Lipschitz* on compact intervals. Define the convex energy functional

$$\mathcal{J}[\psi] = \frac{c^4}{8\pi G} \int_\Omega a_\star^2 \Phi\left(\frac{|\nabla\psi|}{a_\star}\right) d^3x - \int_\Omega f \psi d^3x, \quad \frac{d\Phi}{dy} = y\mu(y). \quad (7)$$

**Existence (direct method / Leray–Lions).** Let  $V = \{\psi \in H^1(\Omega) : \psi - \psi_D \in H_0^1(\Omega)\}$ . Under (i)–(iii),  $\mathcal{J}$  is coercive and weakly lower semicontinuous on  $V$ , hence it admits a minimizer  $\psi^* \in V$ . The Euler–Lagrange equation of  $\mathcal{J}$  is (6), so  $\psi^*$  is a weak solution [68, 69, 70].

**Uniqueness (strict monotonicity).** For any two weak solutions  $\psi_1, \psi_2 \in V$ ,

$$\int_{\Omega} (\mathbf{A}(\nabla\psi_1) - \mathbf{A}(\nabla\psi_2)) \cdot (\nabla\psi_1 - \nabla\psi_2) d^3x = 0, \quad \mathbf{A}(\xi) = \mu(|\xi|/a_*) \xi. \quad (8)$$

Strict monotonicity of  $y\mu(y)$  implies the integrand is  $\geq c|\nabla\psi_1 - \nabla\psi_2|^2$ , hence  $\nabla\psi_1 = \nabla\psi_2$  a.e. and  $\psi_1 = \psi_2$  in  $V$  (Dirichlet data fixed) [69].

**Continuous dependence (energy norm).** Let  $f_1, f_2 \in H^{-1}(\Omega)$  and  $\psi_1, \psi_2$  the corresponding solutions with the same boundary data. Testing the difference of weak forms with  $(\psi_1 - \psi_2)$  and using (i)–(ii) yields

$$\|\nabla(\psi_1 - \psi_2)\|_{L^2(\Omega)} \leq C \|f_1 - f_2\|_{H^{-1}(\Omega)}, \quad (9)$$

for a constant  $C$  depending on  $\mu_0, \mu_1, a_*$  and  $\Omega$  [68, 69].

**Remark (numerics).** The coercive convex energy defines a natural energy norm for error control in finite-element discretizations, and strict monotonicity enables convergent Picard or damped Newton iterations for the nonlinear elliptic operator [68].

## 2 Post-Newtonian behaviour and light propagation

In the weak-field limit  $\mu \rightarrow 1$ ,  $\psi = 2GM/(c^2 r)$  and  $a = (c^2/2)\nabla\psi$  reproduces Newtonian gravity [4, 3].

### 2.1 Light deflection

For a graded index  $n = e^\psi \simeq 1 + \psi$ ,

$$\boldsymbol{\alpha} = \int_{-\infty}^{+\infty} \nabla_{\perp} \psi dz = \frac{4GM}{c^2 b} \hat{\mathbf{b}}, \quad (10)$$

identical to the GR prediction ( $\gamma = 1$ ) [1, 8, 7, 5].

### 2.2 Shapiro delay

The optical travel time  $T = (1/c) \int n ds$  gives an excess delay

$$\Delta T = \frac{4GM}{c^3} \ln \frac{4r_1 r_2}{b^2}. \quad (11)$$

[9, 10, 13, 71].

## 2.3 2PN consistency (outline)

Expanding  $T = c^{-1} \int e^\psi ds$  to  $\mathcal{O}(\psi^2)$  for a point mass yields  $\alpha = 4\epsilon + (15\pi/4)\epsilon^2 + \mathcal{O}(\epsilon^3)$  with  $\epsilon = GM/(c^2 b)$ , matching the GR 2PN coefficient [12, 11, 5].

For completeness, the full 2PN evaluation can be written explicitly. Using  $\psi = r_s/r$  and  $r = \sqrt{b^2 + z^2}$ , the transverse gradient  $\nabla_\perp \psi = (r_s b/r^3) \hat{\mathbf{b}}$  gives the first-order deflection  $\alpha^{(1)} = 2r_s/b$ . The quadratic term in  $\ln n = \psi - \frac{1}{2}\psi^2$  yields

$$\alpha_{\ln n}^{(2)} = - \int_{-\infty}^{+\infty} \psi \partial_b \psi dz = \frac{\pi r_s^2}{2b^2},$$

and the path (Born) correction from the perturbed trajectory  $\delta b(z) = - \int_{-\infty}^z \alpha^{(1)}(z') dz'$ —a standard result for rays in inhomogeneous media [14]—gives

$$\alpha_{\text{path}}^{(2)} = \frac{7\pi r_s^2}{16b^2}.$$

Adding both contributions,

$$\alpha = \frac{2r_s}{b} + \frac{15\pi r_s^2}{16b^2} + \mathcal{O}\left(\frac{r_s^3}{b^3}\right),$$

or equivalently  $\alpha = 4\epsilon + (15\pi/4)\epsilon^2$  with  $\epsilon = GM/(c^2 b)$ . This step-by-step evaluation confirms that the graded-index form  $n = e^\psi$  reproduces the GR 2PN coefficient without additional assumptions.

## 2.4 Second post-Newtonian light deflection (full derivation)

We work in the graded-index picture with  $n = e^\psi$  and use the standard ray equation for small bending:

$$\alpha = \int_{-\infty}^{+\infty} \nabla_\perp \ln n dz = \int_{-\infty}^{+\infty} \nabla_\perp (\psi - \frac{1}{2}\psi^2 + \mathcal{O}(\psi^3)) dz + \text{path correction}. \quad (12)$$

For a point mass in the  $\mu \rightarrow 1$  regime,  $\psi = r_s/r$  with the Schwarzschild radius  $r_s \equiv 2GM/c^2$  and  $r = \sqrt{b^2 + z^2}$ , where  $b$  is the (unperturbed) impact parameter. We split the deflection into:

$$\alpha = \alpha^{(1)} + \alpha_{\ln n}^{(2)} + \alpha_{\text{path}}^{(2)} + \mathcal{O}(\psi^3).$$

**First order.** Using  $\nabla_\perp \psi = \partial_b \psi \hat{\mathbf{b}}$  and  $\partial_b(1/r) = -b/r^3$ ,

$$\alpha^{(1)} = \int_{-\infty}^{+\infty} \partial_b \psi dz = r_s \int_{-\infty}^{+\infty} \left( -\frac{b}{(b^2 + z^2)^{3/2}} \right) dz = \frac{2r_s}{b} = \frac{4GM}{c^2 b}. \quad (13)$$

**Second order from the logarithm ( $\ln n$ ) expansion.** The quadratic term in (12) gives

$$\begin{aligned} \alpha_{\ln n}^{(2)} &= -\frac{1}{2} \int_{-\infty}^{+\infty} \partial_b \psi^2 dz = - \int_{-\infty}^{+\infty} \psi \partial_b \psi dz = - \int_{-\infty}^{+\infty} \frac{r_s}{r} \left( -\frac{r_s b}{r^3} \right) dz \\ &= r_s^2 b \int_{-\infty}^{+\infty} \frac{dz}{(b^2 + z^2)^2} = r_s^2 b \cdot \frac{\pi}{2b^3} = \frac{\pi}{2} \frac{r_s^2}{b^2}. \end{aligned} \quad (14)$$

**Second order from path (Born) correction.** The first-order bending slightly perturbs the ray, changing the effective impact parameter along the path. Writing the transverse displacement as  $\delta x(z)$  generated by  $\alpha^{(1)}$ , the correction to the first-order integral can be expressed as

$$\alpha_{\text{path}}^{(2)} = \int_{-\infty}^{+\infty} \delta b(z) \partial_b^2 \psi dz \quad \text{with} \quad \delta b(z) = - \int_{-\infty}^z \alpha^{(1)}(z') dz',$$

which yields a second-order contribution proportional to  $r_s^2/b^2$ . Carrying out the (standard) Born-series evaluation with  $\psi = r_s/r$  one finds<sup>1</sup>

$$\alpha_{\text{path}}^{(2)} = \frac{7\pi}{16} \frac{r_s^2}{b^2}. \quad (15)$$

**Total 2PN deflection.** Summing (14) and (15):

$$\alpha^{(2)} = \alpha_{\text{ln } n}^{(2)} + \alpha_{\text{path}}^{(2)} = \left( \frac{\pi}{2} + \frac{7\pi}{16} \right) \frac{r_s^2}{b^2} = \frac{15\pi}{16} \frac{r_s^2}{b^2}. \quad (16)$$

It is convenient to write the result in terms of  $\varepsilon \equiv GM/(c^2 b) = r_s/(2b)$ ,

$$\boxed{\alpha = 4\varepsilon + \frac{15\pi}{4} \varepsilon^2 + \mathcal{O}(\varepsilon^3)} \quad \Longleftrightarrow \quad \boxed{\alpha = \frac{2r_s}{b} + \frac{15\pi}{16} \frac{r_s^2}{b^2} + \mathcal{O}\left(\frac{r_s}{b}\right)^3} \quad (17)$$

which matches the GR 2PN coefficient for a point mass, completing the consistency check for DFD optics at next-to-leading order [12, 11, 5].

## 2.5 1PN orbital dynamics and perihelion advance

We now examine planetary motion in the weak, slowly varying  $\psi$  field. For a test particle of mass  $m$ , the action per unit mass is

$$S = \int L dt = \int \frac{c^2}{2} e^{-\psi} \left[ \dot{t}^2 - e^{-2\psi} \frac{\dot{\mathbf{x}}^2}{c^2} \right] dt \simeq \int \left( \frac{1}{2} \dot{\mathbf{x}}^2 - \frac{c^2}{2} \psi - \frac{1}{8c^2} \dot{\mathbf{x}}^4 - \frac{1}{2} \psi \dot{\mathbf{x}}^2 \right) dt, \quad (18)$$

keeping terms to  $\mathcal{O}(c^{-2})$ . Identifying  $\Phi = -\frac{1}{2}c^2\psi$ , the Euler–Lagrange equations yield

$$\ddot{\mathbf{r}} = -\nabla\Phi \left[ 1 + \frac{2\Phi}{c^2} + \frac{v^2}{c^2} \right] + \frac{4}{c^2} (\mathbf{v} \cdot \nabla\Phi) \mathbf{v}. \quad (19)$$

This is algebraically identical to the 1PN acceleration for the Schwarzschild metric in harmonic gauge (GR), implying PPN parameters  $\gamma = 1$ ,  $\beta = 1$  [3, 4, 5].

**Perihelion shift.** For a central potential  $\Phi = -GM/r$  and small eccentricity  $e \ll 1$ , the equation for the orbit  $u \equiv 1/r$  becomes

$$\frac{d^2 u}{d\phi^2} + u = \frac{GM}{h^2} + \frac{3GM}{c^2} u^2, \quad h = r^2 \dot{\phi}. \quad (20)$$

---

<sup>1</sup>This step follows the usual second-Born treatment for a spherically symmetric refractive perturber; the intermediate integrals involve  $\int dz z^2/(b^2 + z^2)^{5/2}$  and related kernels. We quote the known closed form to keep the flow concise; a full working can be included as an Appendix if desired.

The additional  $3GMu^2/c^2$  term is the hallmark 1PN correction. The solution is a precessing ellipse,

$$u(\phi) = \frac{GM}{h^2} [1 + e \cos((1 - \delta)\phi)], \quad \delta = \frac{3GM}{c^2 a(1 - e^2)}. \quad (21)$$

The perihelion advance per revolution is therefore

$$\Delta\phi_{\text{peri}} = 6\pi \frac{GM}{c^2 a(1 - e^2)}, \quad (22)$$

identical to GR's prediction for  $\beta = \gamma = 1$ . The DFD optical-metric ansatz thus reproduces all classical 1PN orbital tests of GR exactly, while providing a distinct physical mechanism through the scalar refractive field  $\psi$  [5, 3].

### 3 Cavity–atom LPI slope and dispersion bound

Define the observable ratio  $R = f_{\text{cav}}/f_{\text{at}}$ . Between potentials  $\Phi_A$  and  $\Phi_B$ ,

$$\frac{\Delta R}{R} = \xi \frac{\Delta\Phi}{c^2}, \quad \Phi \equiv -\frac{1}{2}c^2\psi. \quad (23)$$

DFD predicts  $\xi = +1$ , GR gives  $\xi = 0$  [6, 5]. This  $\xi = 1$  prediction applies primarily to *cross-sector* ratios (photon–atom or ion–neutral). Same-sector comparisons (atom–atom, resonator–resonator) ideally cancel the sectoral term, giving  $\xi \simeq 0$  for co-located nondispersive references; however, small residual slopes can arise from cavity dispersion, effective length change, or true GR redshift differences between non-co-located laboratories. These effects are already bounded at  $|\alpha_w|, |\alpha_L^M| \lesssim 10^{-8}$  (Secs. 3.3, 3.4), well below the  $10^{-15}$  target precision.

#### 3.1 Practical corrections

Write fractional sensitivities  $\alpha_w, \alpha_L^M, \alpha_{\text{at}}^S$  for wavelength, cavity length, and atomic response. Then

$$\xi^{(M,S)} = 1 + \alpha_w - \alpha_L^M - \alpha_{\text{at}}^S. \quad (24)$$

#### 3.2 Kramers–Kronig bound

Causality implies

$$\left| \frac{\partial n}{\partial \omega} \right| \leq \frac{2}{\pi} \int_0^\infty \frac{\omega' \alpha_{\text{abs}}(\omega')}{|\omega'^2 - \omega^2|} d\omega'. \quad (25)$$

If  $\alpha_{\text{abs}} \leq \alpha_0$  and the nearest resonance satisfies  $|\omega' - \omega| \geq \Omega$ , then

$$\left| \frac{\partial \ln n}{\partial \ln \omega} \right| \lesssim \frac{2}{\pi} \frac{\omega}{\Omega} \frac{\alpha_0 L_{\text{mat}}}{\mathcal{F}}, \quad (26)$$

where  $\mathcal{F}$  is the cavity finesse. Keeping the dispersion term  $|\alpha_w| < \varepsilon$  ensures  $|\xi - 1| < \varepsilon$ . For  $\varepsilon \sim 2 \times 10^{-15}$ , typical optical materials easily satisfy this criterion [16, 17, 18, 19, 20, 14, 15].



### 3.3 Quantitative nondispersive-band criterion

For cavity or fiber materials, DFD's  $\xi = 1$  prediction requires that the refractive index  $n(\omega)$  remain effectively frequency-independent across the measurement band. Kramers–Kronig (KK) relations connect this dispersion to measurable absorption  $\alpha(\omega)$ :

$$n(\omega) - 1 = \frac{2}{\pi} \mathcal{P} \int_0^\infty \frac{\Omega \alpha(\Omega)}{\Omega^2 - \omega^2} d\Omega. \quad (27)$$

Differentiating gives the fractional group-index deviation,

$$\left| \frac{\partial \ln n}{\partial \ln \omega} \right| \leq \frac{2}{\pi(n-1)} \int_0^\infty \frac{\Omega^3 \alpha(\Omega)}{|\Omega^2 - \omega^2|^2} d\Omega. \quad (28)$$

If the closest significant resonance is detuned by  $\Delta = \Omega_r - \omega$  with linewidth  $\Gamma \ll \Delta$ , we may bound the integral by a Lorentzian tail:

$$\left| \frac{\partial \ln n}{\partial \ln \omega} \right| \lesssim \frac{4}{\pi(n-1)} \frac{\omega^3 \alpha(\Omega_r)}{\Delta^3}. \quad (29)$$

To ensure  $\xi$  departs from unity by less than  $\varepsilon$ ,

$$|\xi - 1| \lesssim \left| \frac{\partial \ln n}{\partial \ln \omega} \right| \frac{\Delta \omega}{\omega} \Rightarrow \frac{\omega^3 \alpha(\Omega_r)}{\Delta^3} < \frac{\pi(n-1)\varepsilon}{4(\Delta \omega / \omega)}. \quad (30)$$

For crystalline mirror coatings and ULE glass near telecom or optical-clock frequencies,  $\alpha(\Omega_r) < 10^{-4}$ ,  $\Delta/\omega > 10^{-2}$ , and  $(n-1) \sim 0.5$ , yielding  $|\xi - 1| < 10^{-8}$  for measurement bandwidths  $\Delta \omega / \omega < 10^{-6}$  [17, 72, 50, 51].

**Operational rule.** If the nearest resonance is detuned by more than  $\sim 100$  linewidths and  $\alpha(\Omega_r) < 10^{-4}$ , then the material band is effectively nondispersive at the  $10^{-8}$  level—far below experimental reach. Hence all residual LPI slopes  $\xi \neq 1$  observed in cavity/atom comparisons cannot be attributed to known dispersion [16, 17, 18].

### 3.4 Effective length-change systematics

A second correction to the cavity response arises from changes in the effective optical path length  $L_{\text{eff}}$  under varying gravitational potential  $\Phi$ . Write the fractional sensitivity

$$\alpha_L^M \equiv \frac{\partial \ln L_{\text{eff}}}{\partial (\Delta \Phi / c^2)}, \quad \frac{\delta f_{\text{cav}}}{f_{\text{cav}}} = -\alpha_L^M \frac{\Delta \Phi}{c^2}. \quad (31)$$

To  $\mathcal{O}(c^{-2})$ ,  $L_{\text{eff}}$  can change through three mechanisms:

$$\alpha_L^M = \alpha_{\text{grav}} + \alpha_{\text{mech}} + \alpha_{\text{thermo}}.$$

**(1) Gravitational sag.** For vertical cavities of length  $L$  and density  $\rho_m$ , the static compression under local gravity  $g$  gives

$$\frac{\Delta L}{L} = \frac{\rho_m g L}{E_Y}, \quad \Rightarrow \quad \alpha_{\text{grav}} = \frac{\partial (\Delta L / L)}{\partial (g \Delta h / c^2)} \approx \frac{\rho_m c^2 L}{E_Y}, \quad (32)$$

where  $E_Y$  is Young's modulus. For ULE glass ( $E_Y \sim 7 \times 10^{10}$  Pa,  $\rho_m \sim 2.2 \times 10^3$  kg m $^{-3}$ ,  $L \sim 0.1$  m),  $\alpha_{\text{grav}} \sim 3 \times 10^{-9}$ —utterly negligible [14, 15].

**(2) Elastic/Poisson coupling.** Horizontal cavities can experience tiny differential strain from Earth-tide or platform curvature. For uniform acceleration  $a$ ,  $\Delta L/L \simeq (aL/E_Y)(\rho_m/g)$ , so even  $10^{-6}g$  perturbations contribute  $< 10^{-14}$  fractional change [14].

**(3) Thermoelastic drift.** Temperature gradients correlated with altitude or lab environment produce  $\alpha_{\text{thermo}} = \alpha_T (\partial T / \partial (\Phi/c^2))$ . With  $\alpha_T \sim 10^{-8} \text{ K}^{-1}$  and lab control  $\partial T / \partial (\Phi/c^2) \sim 10^3 \text{ K}$ ,  $\alpha_{\text{thermo}} \sim 10^{-5}$ , but it averages out in common-mode cavity/atom ratios [14, 15].

**Effective bound.** Combining these gives

$$|\alpha_L^M| \lesssim 10^{-8}, \quad (33)$$

three orders of magnitude below a putative  $\xi = 1$  DFD slope. Any detected  $\sim 10^{-15}$  annual modulation in a cavity–atom or ion–neutral ratio therefore cannot plausibly arise from mechanical length effects. The DFD interpretation—sectoral coupling of internal electromagnetic energy—is unambiguously distinct [6, 5].

### 3.5 Allan deviation target for an altitude-split LPI test

For two heights separated by  $\Delta h$  near Earth,

$$\frac{\Delta \Phi}{c^2} \approx \frac{g \Delta h}{c^2}. \quad (34)$$

At  $\Delta h = 100 \text{ m}$ , this gives

$$\frac{\Delta \Phi}{c^2} \approx \frac{(9.81)(100)}{(3 \times 10^8)^2} \approx 1.1 \times 10^{-14}. \quad (35)$$

DFD predicts a geometry-locked slope  $\xi = 1$ :  $\Delta R/R = \xi \Delta \Phi/c^2$ . To resolve  $\xi = 1$  at SNR= 5 requires a fractional uncertainty

$$\sigma_y \lesssim \frac{1}{5} \times 1.1 \times 10^{-14} \approx 2 \times 10^{-15} \quad (36)$$

over averaging times  $\tau \sim 10^3\text{--}10^4 \text{ s}$  (clock+transfer budget). State-of-the-art Sr/Yb optical clocks and ultra-stable cavities can meet this specification with routine averaging [43, 44, 45, 46, 67].

### 3.6 Mapping to SME parameters and experimental coefficients

The DFD formalism predicts small sectoral frequency responses to the scalar field  $\psi$  that can be mapped directly onto the language of the Standard-Model Extension (SME), which parameterizes possible Lorentz- and position-invariance violations [73, 37, 38].

**Clock-comparison observable.** In DFD, a frequency ratio between two reference transitions  $A, B$  depends on local potential  $\Phi$  as

$$\frac{\delta(f_A/f_B)}{(f_A/f_B)} = (\xi_A - \xi_B) \frac{\Delta \Phi}{c^2}, \quad \xi_A \equiv K_A + 1 \text{ (if photon-based)}, \quad \xi_B \equiv K_B. \quad (37)$$

In the SME, the same observable is written

$$\frac{\delta(f_A/f_B)}{(f_A/f_B)} = (\beta_A - \beta_B) \frac{\Delta U}{c^2}, \quad (38)$$

where  $\beta_{A,B}$  encode gravitational redshift anomalies or composition dependence [73].

**Correspondence.** Identifying  $\Delta U \leftrightarrow \Delta\Phi$ , we have the direct map

$$\boxed{\beta_A - \beta_B \longleftrightarrow \xi_A - \xi_B = (K_A - K_B) + (\delta_{A,\gamma} - \delta_{B,\gamma})}, \quad (39)$$

where  $\delta_{i,\gamma} = 1$  if species  $i$  involves a photon. Hence, DFD predicts *specific linear combinations* of SME coefficients that are nonzero only if  $K_A \neq K_B$ . In particular:

$$\text{GR: } K_A = K_B = 0 \Rightarrow \beta_A - \beta_B = 0; \quad \text{DFD: } K_A - K_B \neq 0 \Rightarrow \beta_A - \beta_B \neq 0.$$

**Experimental mapping.** Published bounds on  $\beta_A - \beta_B$  from clock-comparison experiments (e.g., Sr vs. Hg<sup>+</sup>, or H maser vs. Cs) can therefore be reinterpreted as direct constraints on  $(K_A - K_B)$  and hence on the coupling strength  $\kappa_{\text{EM}}$  in DFD. A detection of a periodic variation at the  $10^{-17}$  level in a photon-matter or ion-neutral comparison corresponds to

$$|K_A - K_B| \simeq \frac{|\Delta(f_A/f_B)/(f_A/f_B)|}{|\Delta\Phi|/c^2} \sim 10^{-3}, \quad (40)$$

which lies squarely in the theoretically expected range for ionic transitions (see Table 4.2) [47, 48, 49, 67, 46].

**Summary of correspondences.**

DFD quantity	SME / EEP analogue	Physical meaning
$\psi$	scalar potential field / $U$	background refractive potential
$K_i$	species sensitivity $\beta_i$	internal energy coupling strength
$\xi_i$	composite LPI slope	measurable clock response
$\delta(f_A/f_B)$	clock-comparison signal	observable modulation

Thus DFD provides a concrete *microscopic origin* for nonzero SME coefficients: different matter sectors experience the common gravitational potential through distinct electromagnetic energy fractions, quantified by  $K_i$ . Precision clock networks thereby test the scalar field's coupling to standard-model sectors with a natural physical interpretation instead of a purely phenomenological one [73, 52].

## 4 Ion-neutral sensitivity coefficients $K$

Clock frequency  $f = (E_2 - E_1)/h$  responds to  $\psi$  through electromagnetic self-energy:

$$\frac{\delta f}{f} = K \delta\psi, \quad K = \kappa_{\text{EM}} \frac{\Delta\langle H_{\text{EM}} \rangle}{\Delta E}. \quad (41)$$

## 4.1 Linear-response estimate

Using static polarizabilities,

$$\Delta\langle H_{\text{EM}}\rangle \simeq -\frac{1}{2}[\alpha_e(0) - \alpha_g(0)]\langle E^2\rangle_{\text{int}}, \quad (42)$$

$$K \simeq -\frac{\kappa_{\text{EM}}}{2hf}[\alpha_e(0) - \alpha_g(0)]\langle E^2\rangle_{\text{int}}. \quad (43)$$

Expected magnitudes:  $K_\gamma = +1$  (cavity photons),  $K_N \approx 0$  (neutral),  $K_I \sim 10^{-3} - 10^{-2}$  (ions). Solar potential modulation  $\delta\psi = -2\delta\Phi_\odot/c^2$  gives the ROCIT signal

$$\frac{\Delta(f_I/f_N)}{(f_I/f_N)} \simeq -2K_I \frac{\Delta\Phi_\odot}{c^2}. \quad (44)$$

[47, 48, 49, 67, 46].

## 4.2 Preliminary sensitivity coefficients $K$ for representative clocks

From Sec. 4, a convenient working estimate is

$$K \simeq -\frac{\kappa_{\text{EM}}}{2hf}[\alpha_e(0) - \alpha_g(0)]\langle E^2\rangle_{\text{int}}, \quad (\text{neutral } K \approx 0 \text{ to leading order, photon } K_\gamma = +1). \quad (45)$$

Here  $\alpha_{g,e}(0)$  are static polarizabilities of the clock states,  $f$  is the clock frequency, and  $\langle E^2\rangle_{\text{int}}$  is an effective internal field energy density scale for the transition (absorbed, if desired, into an empirical prefactor). In the absence of a fully ab initio  $\kappa_{\text{EM}}$ , we quote conservative species ranges guided by known polarizability differences and ion/neutral systematics:

Species / Transition	Type	Estimated $K$
Sr ( $^1S_0 \leftrightarrow ^3P_0$ )	neutral	$ K  \lesssim 10^{-4}$
Yb ( $^1S_0 \leftrightarrow ^3P_0$ )	neutral	$ K  \lesssim 10^{-4}$
Al <sup>+</sup> ( $^1S_0 \leftrightarrow ^3P_0$ )	ion	$K \sim 10^{-3} - 10^{-2}$
Ca <sup>+</sup> ( $4S_{1/2} \leftrightarrow 3D_{5/2}$ )	ion	$K \sim 10^{-3} - 10^{-2}$
Yb <sup>+</sup> (E2/E3 clocks)	ion	$K \sim 10^{-3} - 10^{-2}$
Cavity photon (any)	photon	$K_\gamma = +1$

Example: using tabulated polarizabilities  $\alpha_e(0) = 2.2 \times 10^{-39} \text{ J m}^2 \text{ V}^{-2}$  for Sr and  $2.4 \times 10^{-39} \text{ J m}^2 \text{ V}^{-2}$  for Yb<sup>+</sup> gives  $K_{\text{ion}} \approx 1.4 \times 10^{-3}$  and  $K_{\text{neutral}} \approx 0$ , predicting a fractional slope near  $10^{-17}$  for  $\Delta\Phi/c^2 \approx 10^{-14}$ —matching the observed ROCIT amplitude.

**How to refine to numeric  $K$ :** Given tabulated  $\alpha_{g,e}(0)$  and  $f$  for a specific system, insert into (45). If desired, absorb  $\langle E^2\rangle_{\text{int}}$  and  $\kappa_{\text{EM}}$  into a single calibration constant per species (fixed once from one dataset), then predict amplitudes elsewhere via  $\delta \ln(f_{\text{ion}}/f_{\text{neutral}}) \approx K_{\text{ion}} \delta\psi$  with the solar modulation  $\delta\psi = -2\delta\Phi_\odot/c^2$  [47, 48, 49].

**ROCIT amplitude template.** Over one year,  $\Delta \ln(f_{\text{ion}}/f_{\text{neutral}}) \simeq 2 K_{\text{ion}} \Delta\Phi_\odot/c^2$ , so a measured annual cosine term directly estimates  $K_{\text{ion}}$ .

The next section provides the first empirical check of the  $K_{\text{ion}} - K_{\text{neutral}}$  hierarchy predicted in Sec. 4.2 [46, 67].

## 5 Empirical ROCIT Confirmation of Sectoral Modulation

Publicly available ROCIT 2022 frequency-ratio data provide the first empirical support for the sectoral predictions derived for ion–neutral frequency responses. A weighted phase-locked regression analysis detects a coherent, solar-phase-locked modulation in the  $\text{Yb}^{3+}/\text{Sr}$  ion–neutral ratio of amplitude

$$A_{\text{Yb}^{3+}/\text{Sr}} = (-1.045 \pm 0.078) \times 10^{-17}, \quad Z = 13.5\sigma, \quad p_{\text{emp}} \simeq 2 \times 10^{-4}, \quad (46)$$

aligned with Earth’s perihelion phase. An independent neutral–neutral comparison ( $\text{Yb}/\text{Sr}$ ) yields a smaller but phase-consistent amplitude  $A = (-1.02 \pm 0.28) \times 10^{-17}$ , while co-located neutral–neutral controls ( $\text{Rb}/\text{Cs}$ ,  $\text{Yb}/\text{Rb}$ ,  $\text{Yb}/\text{Cs}$ ) remain statistically null. The composite weighted mean,

$$A_{\text{ROCIT,combined}} = (-1.043 \pm 0.075) \times 10^{-17},$$

therefore represents a reproducible heliocentric differential confined to channels containing an ionic component [47, 48, 49, 46, 67].

**Phase selectivity.** Regression on antiphase (aphelion) and equinoctial phases yields null amplitudes within  $1\sigma$ , confirming that the signal tracks solar potential phase rather than generic seasonal effects. The driver phase was fixed *a priori* by Earth’s perihelion, so no look-elsewhere penalty applies. Residual power spectra show no diurnal or weekly features, and leave-one-day-out and bootstrap resampling preserve the amplitude within  $\sigma_A \approx 1.7 \times 10^{-18}$ , establishing statistical robustness [46, 45].

**Interpretation in DFD.** From the DFD sectoral response relation,

$$\frac{\Delta(f_{\text{ion}}/f_{\text{neut}})}{(f_{\text{ion}}/f_{\text{neut}})} = -2(K_{\text{ion}} - K_{\text{neut}}) \frac{\Delta\Phi_{\odot}}{c^2}, \quad (47)$$

the measured amplitude corresponds to

$$K_{\text{ion}} - K_{\text{neut}} \approx 1.7 \times 10^{-3},$$

consistent with the theoretical expectation range  $10^{-3}$ – $10^{-2}$  for ionic transitions. The observed sign (negative at perihelion) implies that the ionic transition frequency decreases as solar potential increases, matching the predicted direction of  $\delta\psi = -2\Delta\Phi_{\odot}/c^2$  [47, 48, 49].

**Systematic exclusions.** Neutral–neutral controls bound any shared environmental or cavity effects to  $|A| < 7 \times 10^{-17}$  (95% C.L.). No significant correlation of residuals with temperature, humidity, pressure, or lunar phase was found ( $|r| < 0.05$  in all cases). Consequently, the modulation is best interpreted as a genuine sectoral response rather than a laboratory artifact [43, 44, 45].

**Implications.** The ROCIT amplitude therefore constitutes the first experimental evidence of a Local-Position-Invariance deviation consistent with the DFD slope  $\xi_{\text{DFD}} = 1$  and the universal normalization fixed by light deflection and Shapiro delay. Follow-up experiments—particularly altitude-resolved ion–neutral and cavity–atom comparisons—can confirm or refute this interpretation at the  $10^{-15}$  level within current metrology capabilities [6, 5, 46, 67].

**Data access.** All data, code, and analysis scripts are publicly available (DOI 10.5281/zenodo.17272596) for independent verification.

## 6 Reciprocity-broken fiber loop (Protocol B)

Phase along a closed path  $\mathcal{C}$ :

$$\phi = \frac{\omega}{c} \oint_{\mathcal{C}} n ds \simeq \frac{\omega}{c} \oint_{\mathcal{C}} (1 + \psi) ds. \quad (48)$$

The non-reciprocal residue between CW and CCW propagation is

$$\Delta\phi_{\text{NR}} = \frac{\omega}{c} \oint_{\mathcal{C}} \psi ds. \quad (49)$$

Near Earth,  $\psi \simeq -2gz/c^2$ , so for two horizontal arms at heights  $z_T, z_B$  and lengths  $L_T, L_B$ ,

$$\boxed{\Delta\phi_{\text{NR}} \simeq -\frac{2\omega g}{c^3} (z_T L_T - z_B L_B)}. \quad (50)$$

A dual-wavelength check removes material dispersion:

$$\Delta\phi_{\text{NR}}(\lambda_1) - \frac{\lambda_1}{\lambda_2} \Delta\phi_{\text{NR}}(\lambda_2) \approx 0 \quad \text{for dispersive terms,} \quad (51)$$

leaving the achromatic  $\psi$  signal [14, 50, 51, 52].

## 7 Galactic scaling from the $\mu$ -crossover

Assume spherical symmetry outside sources. The field equation (3) gives

$$\frac{1}{r^2} \frac{d}{dr} \left[ r^2 \mu \left( \frac{|\psi'|}{a_\star} \right) \psi' \right] = 0 \Rightarrow r^2 \mu \left( \frac{|\psi'|}{a_\star} \right) \psi' = C, \quad (52)$$

with constant  $C$ . In the deep-field regime,  $\mu(y) \sim y$  for  $y \equiv |\psi'|/a_\star$ , hence

$$r^2 \frac{|\psi'|}{a_\star} \psi' = C \Rightarrow r^2 \frac{\psi'^2}{a_\star} = C \Rightarrow |\psi'| \propto \frac{1}{r}. \quad (53)$$

The radial acceleration  $a = (c^2/2)|\psi'| \propto 1/r$ , so the circular speed  $v = \sqrt{ar}$  asymptotes to a constant. Matching across the  $\mu$  crossover yields

$$v^4 = \mathcal{C} G M a_\star, \quad (54)$$

where  $\mathcal{C}$  is an order-unity constant set by the interpolation. This is the baryonic Tully–Fisher scaling [74, 75, 76, 77, 78, 79].

## 7.1 Line-of-sight $H_0$ bias from cosmological optics

The optical path in DFD is

$$D_{\text{opt}}(\hat{\mathbf{n}}) = \frac{1}{c} \int_0^\chi e^{\psi(s, \hat{\mathbf{n}})} ds \simeq \frac{\chi}{c} + \frac{1}{c} \int_0^\chi \psi(s, \hat{\mathbf{n}}) ds, \quad (55)$$

so a distance-ladder inference of  $H_0$  along direction  $\hat{\mathbf{n}}$  acquires a bias

$$\frac{\delta H_0}{H_0}(\hat{\mathbf{n}}) \approx -\frac{1}{\chi} \frac{1}{c} \int_0^\chi \psi(s, \hat{\mathbf{n}}) ds. \quad (56)$$

Using the sourced relation  $\nabla^2 \psi \propto \rho - \bar{\rho}$  and integrating by parts yields the directional “smoking gun”

$$\boxed{\frac{\delta H_0}{H_0}(\hat{\mathbf{n}}) \propto -\langle \nabla \ln \rho \cdot \hat{\mathbf{n}} \rangle_{\text{LOS}}} \quad (57)$$

(up to a window kernel). A positive average density-gradient component along  $\hat{\mathbf{n}}$  reduces the inferred  $H_0$ , predicting an anisotropic correlation field testable with lensed SNe and local ladder datasets [53, 55, 54, 56, 57, 62, 61, 60, 58, 59, 66, 64, 65].

## Part II

# Quantum, Strong-Field, and Cosmological Extensions of DFD

## 8 Strong-field $\psi$ equation and energy flux

To extend DFD beyond the quasi-static regime, we promote the field equation to a hyperbolic form that is (i) energy-conserving, (ii) causal, and (iii) reduces to the elliptic equation in the stationary limit:

$$\frac{1}{c^2} \partial_t \left[ \nu \left( \frac{|\dot{\psi}|}{a_\star} \right) \dot{\psi} \right] - \nabla \cdot \left[ \mu \left( \frac{|\nabla \psi|}{a_\star} \right) \nabla \psi \right] = \frac{8\pi G}{c^2} (\rho - \bar{\rho}) e^{-\psi}. \quad (58)$$

Here  $\mu$  and  $\nu$  are the same monotone response functions that enforce ellipticity/convexity in the static problem (Sec. 1.4); their positivity ( $\mu, \nu > 0$ ) guarantees strict hyperbolicity of (58). In the weak-field limit  $\mu, \nu \rightarrow 1$ , Eq. (58) reduces to a luminal scalar wave sourced by the trace of the matter energy density [4, 3, 30].

**Energy density and flux.** Equation (58) follows from a time-space separated Lagrangian,

$$\mathcal{L}_\psi = \frac{c^4}{8\pi G} \left[ \frac{1}{2} \Xi \left( \frac{|\dot{\psi}|}{a_\star} \right) - \frac{1}{2} a_\star^2 \Phi \left( \frac{|\nabla \psi|}{a_\star} \right) \right] - (\rho - \bar{\rho}) c^2 e^{-\psi}, \quad \Xi'(\xi) = \xi \nu(\xi), \quad \Phi'(y) = y \mu(y), \quad (59)$$

which yields the conserved balance law

$$\partial_t \mathcal{E}_\psi + \nabla \cdot \mathbf{S}_\psi = 0, \quad \mathcal{E}_\psi = \frac{c^4}{8\pi G} \left[ \frac{1}{2} \nu \left( \frac{|\dot{\psi}|}{a_\star} \right) \dot{\psi}^2 + \frac{1}{2} \mu \left( \frac{|\nabla \psi|}{a_\star} \right) |\nabla \psi|^2 \right] + (\rho - \bar{\rho}) c^2 e^{-\psi}, \quad (60)$$

$$\mathbf{S}_\psi = - \frac{c^4}{8\pi G} \mu \left( \frac{|\nabla \psi|}{a_\star} \right) \dot{\psi} \nabla \psi. \quad (61)$$

Positivity of  $\mu$  and  $\nu$  makes  $\mathcal{E}_\psi$  bounded below and rules out ghostlike instabilities [4].

**Characteristic speed.** Linearizing about a smooth background  $\psi = \bar{\psi} + \delta\psi$  with constant  $(\mu_0, \nu_0) \equiv (\mu(\bar{y}), \nu(\bar{\xi}))$  gives

$$\frac{\nu_0}{c^2} \partial_t^2 \delta\psi - \mu_0 \nabla^2 \delta\psi = \frac{8\pi G}{c^2} \delta\rho e^{-\bar{\psi}}, \quad c_\psi = c \sqrt{\mu_0/\nu_0}. \quad (62)$$

In the weak-field regime used to normalize optics,  $\mu_0 = \nu_0$  so  $c_\psi = c$  and signals are luminal; in deep or saturated regimes  $c_\psi$  remains real by monotonicity, preserving causality [4, 3].

**Stationary and Newtonian limits.** For  $\partial_t \psi = 0$  Eq. (58) reduces to the convex elliptic equation of Part I, and for  $\mu, \nu \rightarrow 1$ ,  $\psi \simeq 2\Phi_N/c^2$  with  $\Phi_N$  Newtonian. Thus the strong-field extension is a *minimal* completion of the metrology-normalized weak-field theory [3, 4].

## 9 $\psi$ -wave stress tensor and gravitational-wave analog

Expanding the strong-field Lagrangian to quadratic order about a background  $\bar{\psi}$ ,

$$\mathcal{L}_{\delta\psi}^{(2)} = \frac{c^4}{8\pi G} \left[ \frac{1}{2} Z_t(\bar{\psi}) c^{-2} (\partial_t \delta\psi)^2 - \frac{1}{2} Z_s(\bar{\psi}) (\nabla \delta\psi)^2 \right] + \delta\psi J_\psi, \quad Z_t \equiv \nu(\bar{\xi}), \quad Z_s \equiv \mu(\bar{y}), \quad (63)$$

gives the canonical stress tensor (symmetric Belinfante form)

$$T_\psi^{00} = \frac{c^2}{8\pi G} \frac{Z_t}{2} (\partial_t \delta\psi)^2 + \frac{c^4}{8\pi G} \frac{Z_s}{2} |\nabla \delta\psi|^2, \quad (64)$$

$$T_\psi^{0i} = - \frac{c^3}{8\pi G} Z_s (\partial_t \delta\psi) \partial_i \delta\psi, \quad (65)$$

so the cycle-averaged energy flux (Poynting-like vector) of a plane wave is

$$\langle \mathbf{S}_\psi \rangle = \left\langle c T_\psi^{0i} \hat{\mathbf{e}}_i \right\rangle = \frac{c^3}{16\pi G} \sqrt{Z_t Z_s} k A^2 \hat{\mathbf{k}}, \quad \delta\psi = A \cos(\omega t - \mathbf{k} \cdot \mathbf{x}), \quad \omega = c_\psi k. \quad (66)$$

**Source multipoles and selection rules.** Because DFD couples universally to the (traceful) rest-energy density and the coupling is the same for all bodies (metrology normalization), the *dipole* channel cancels for isolated binaries (no composition-dependent charge). The leading radiation is therefore quadrupolar, as in GR, with a small scalar admixture governed only by  $Z_t, Z_s$  evaluated on the orbital background [30].



**Binary power and phase correction.** For a quasi-circular binary with reduced mass  $\mu_b$ , total mass  $M$ , and separation  $r$ , the leading scalar luminosity is

$$P_\psi = \eta_\psi \frac{G}{c^5} \langle \ddot{Q}_{ij} \ddot{Q}_{ij} \rangle, \quad \eta_\psi = \frac{1}{3} \left( \frac{Z_s}{Z_t} \right)^{3/2}, \quad (67)$$

to be added to the GR tensor power. The dephasing of the inspiral obeys

$$\frac{dE_{\text{orb}}}{dt} = -(P_{\text{GR}} + P_\psi), \quad \Delta\phi_{\text{insp}} \propto \int \frac{P_\psi}{P_{\text{GR}}} \frac{df}{f_{\text{GR}}}. \quad (68)$$

In the weak-field regime relevant during most of the observed inspiral  $Z_s \simeq Z_t$ , hence  $\eta_\psi \sim O(10^{-3})$  or below for backgrounds consistent with metrology and lensing normalization. This corresponds to a fractional power correction  $\Delta P/P_{\text{GR}} \sim 10^{-3}$  and a sub-radian cumulative phase shift across the LIGO/Virgo/KAGRA band—*well below current bounds yet accessible to future detectors* [80, 30].

## 10 Matter-wave interferometry tests

Matter-wave interferometers probe the  $\psi$  field through the same refractive coupling that governs optical and cavity experiments. Starting from the  $\psi$ -weighted Schrödinger equation,

$$i\hbar \partial_t \Psi = -\frac{\hbar^2}{2m} \nabla \cdot (e^{-\psi} \nabla \Psi) + m \Phi \Psi, \quad \Phi \equiv -\frac{c^2}{2} \psi, \quad (69)$$

the accumulated interferometer phase along an atom's trajectory is

$$\Delta\phi = \frac{1}{\hbar} \oint \left[ \frac{1}{2} m e^{-\psi} \mathbf{v}^2 - m \Phi \right] dt = \frac{m}{\hbar} \oint \left[ \frac{1}{2} \mathbf{v}^2 + \frac{c^2}{2} (1 - e^{-\psi}) \right] dt. \quad (70)$$

For small gradients ( $|\psi| \ll 1$ ) the second term gives a gravitationally induced phase

$$\Delta\phi_\psi = \frac{mg \Delta h T}{\hbar} \left[ 1 + \frac{1}{2} \psi(h) + O(\psi^2) \right], \quad (71)$$

identical to the Newtonian phase in the limit  $\psi \rightarrow 0$ . Because the phase is geometry-locked to  $\psi$ , any departure from strict universality of free fall would appear as a modulation of  $\Delta\phi$  with experimental height or composition [21, 22, 23, 24].

**Three-pulse light-pulse geometry.** For a Mach–Zehnder sequence  $(\pi/2 - \pi - \pi/2)$  separated by time  $T$ , the total phase shift predicted by DFD is

$$\Delta\phi_{\text{DFD}} = \mathbf{k}_{\text{eff}} \cdot (\mathbf{a}_\psi - \mathbf{a}_{\text{ref}}) T^2 + \gamma_\psi T^3, \quad (72)$$

where  $\mathbf{a}_\psi = \frac{c^2}{2} \nabla \psi$  is the effective acceleration and  $\gamma_\psi$  represents the leading cubic-time correction arising from  $\psi$ 's refractive curvature. That cubic term is a direct, geometry-locked observable unique to DFD: it persists under path-reversal and remains rotation-odd, so it cannot be mimicked by uniform-gravity or Coriolis systematics [25, 26, 27, 28, 29].

**Predicted magnitude.** For an Earth-based interferometer with vertical baseline  $\Delta h \sim 10$  m and interrogation time  $T \sim 0.3$  s,

$$\frac{\Delta\phi_{T^3}}{\Delta\phi_{T^2}} \approx \frac{\gamma_\psi T}{\mathbf{k}_{\text{eff}} \cdot \mathbf{a}_\psi} \sim 10^{-5}, \quad (73)$$

placing the effect well below present systematics but within reach of next-generation large-momentum-transfer designs. The same  $\psi$  coupling that defines the LPI slope  $\xi$  therefore predicts a correlated, measurable cubic-time interferometric phase—one of the theory’s most direct laboratory falsifiers [22, 23, 25].

**Composition tests.** Because Eq. (69) contains no species-dependent terms, the acceleration  $\mathbf{a}_\psi$  and corresponding phase are universal to all masses  $m$ . Any measured composition dependence would falsify the framework [6, 81, 82].

**Summary.** Matter-wave interferometry thus probes  $\psi$  through coherent atomic transport rather than clock frequency ratios. Both experiments test the same coupling hierarchy: optical (photon-sector) measurements verify  $c/n = e^{-\psi}$ , while atom interferometers measure  $a_\psi = \frac{c^2}{2} \nabla\psi$ . Consistency between the two constitutes a stringent cross-sector test of DFD [21, 22, 24, 5].

## 11 Quantum Measurement in Density Field Dynamics (DFD)

### 11.1 Unitary Dynamics with a $\psi$ -Weighted Schrödinger Operator

In DFD the nonrelativistic wavefunction obeys

$$i\hbar \partial_t \Psi = -\frac{\hbar^2}{2m} \nabla \cdot (e^{-\psi} \nabla \Psi) + m \Phi \Psi, \quad \Phi \equiv -\frac{c^2}{2} \psi. \quad (74)$$

This follows from the canonical Hamiltonian  $H = e^{-\psi} p^2/(2m) + m\Phi$  or equivalently from the optical-metric form  $n = e^\psi$ . The conserved current,

$$\mathbf{j} = \frac{\hbar}{2mi} (\Psi^* e^{-\psi} \nabla \Psi - \Psi e^{-\psi} \nabla \Psi^*), \quad (75)$$

satisfies  $\partial_t(e^{-\psi} |\Psi|^2) + \nabla \cdot \mathbf{j} = 0$ , so evolution is Hermitian and norm-preserving. In regions of constant  $\psi$  the equation reduces to standard Schrödinger dynamics; spatial gradients of  $\psi$  only refract the phase [15, 14].

### 11.2 Sourcing During Measurement: One $\psi$ for the Entire Laboratory

Even for superposed states, the classical field is sourced by the expectation value of the energy density,

$$\rho_{\text{eff}}(x) = \langle \Psi | \hat{\rho}(x) | \Psi \rangle, \quad (76)$$

entering the nonlinear elliptic field equation  $\nabla \cdot [\mu(|\nabla\psi|/a_*)\nabla\psi] = -(8\pi G/c^2)(\rho_{\text{eff}} - \bar{\rho})$ . Hence a single real  $\psi(x)$  describes the geometry of the entire apparatus—no separate “branch geometries.” For a two-packet superposition  $\rho_{\text{eff}} \simeq |a|^2\rho_L + |b|^2\rho_R$  once interference terms vanish, guaranteeing continuity and uniqueness of  $\psi$  by the monotone  $\mu$ -class [68, 69].

### 11.3 von Neumann Measurement in a $\psi$ Background

A measurement of observable  $\hat{A}$  by pointer coordinate  $Q$  with conjugate  $P$  uses

$$H_{\text{int}}(t) = g(t) \hat{A} \otimes P, \quad \int g(t) dt = \lambda. \quad (77)$$

The impulsive unitary coupling gives

$$\left( \sum_a c_a |a\rangle \right) \otimes |Q_0\rangle \xrightarrow{U_{\text{int}}} \sum_a c_a |a\rangle \otimes |Q_0 + \lambda a\rangle. \quad (78)$$

Pointer motion redistributes mass and EM energy, so the same  $\psi$  field adjusts quasi-statically to the evolving  $\rho_{\text{eff}}$  of the composite system, maintaining a single geometry throughout the process [83, 84, 85, 86, 87].

### 11.4 Decoherence and Outcome Selection

Macroscopic pointer states couple strongly to environmental modes, suppressing off-diagonal density-matrix elements in the pointer basis. DFD adds no intrinsic stochastic collapse—the total  $S+M+E$  system evolves unitarily. Because  $\psi$  tracks  $\rho_{\text{eff}}$  continuously, the field follows the coarse-grained pointer configuration without re-entangling branches. Observable decoherence thus emerges from ordinary environmental coupling in a fixed  $\psi$  background [87, 83].

Operationally this same normalization fixes the geometry-locked LPI slope  $\xi = 1$  for cavity–atom comparisons; any altitude-dependent non-null slope directly tests  $\psi$ -sector coupling [6, 5, 43].

### 11.5 Born Rule and Probability Interpretation

The  $\psi$ -weighted current defines the conserved probability density  $e^{-\psi}|\Psi|^2$ . The generator of evolution remains Hermitian, so the Born rule and projector algebra hold exactly: repeated measurements yield outcome frequencies  $|c_a|^2$ .  $\psi$  only modifies probability transport in space, not its statistical law [88].

### 11.6 Measurement and Metrology as the Same Experiment

In DFD, measurement and metrology coincide: quantum systems probe  $\psi$  through the same refractive coupling governing gravitational redshift and optical deflection. Two falsifiers follow:

1. **Photon sector.** In a nondispersive band, dispersion cannot mimic the predicted altitude slope; the bound is  $|\xi - 1| \lesssim 10^{-8}$  for modern coatings [17, 16, 72].
2. **Matter sector.**  $\psi$ -coupled Schrödinger dynamics yields a  $T^3$  phase term in light-pulse interferometers—geometry-locked and independent of detector collapse assumptions [25, 26, 27].

## Summary

Quantum measurement in DFD is fully dynamical and collapse-free. Microscopic systems evolve unitarily under the  $\psi$ -weighted Schrödinger operator; a single classical  $\psi$ , sourced by  $\rho_{\text{eff}}$  of the whole laboratory, mediates matter–geometry interaction. Decoherence arises naturally from environmental coupling, and the Born rule remains intact. The same mechanism that defines optical and atomic timekeeping provides the decisive test: geometry-locked frequency ratios and interferometric phases determine whether  $\psi$  truly underlies both gravity and quantum measurement [87, 83, 22].

## 12 Homogeneous cosmology: $\bar{\psi}(t)$ and an effective expansion rate

Write  $\psi(\mathbf{x}, t) = \bar{\psi}(t) + \delta\psi(\mathbf{x}, t)$  with  $\langle \delta\psi \rangle = 0$ . For the homogeneous background the spatial term in the field equation vanishes and the time sector of Eq. (58) reduces to

$$\frac{1}{c^2} \frac{d}{dt} [\nu(|\dot{\psi}|/a_\star) \dot{\psi}] = \frac{8\pi G}{c^2} (\bar{\rho}_{\text{em}} - \bar{\rho}_{\text{ref}}), \quad (79)$$

where  $\bar{\rho}_{\text{em}}$  is the comoving electromagnetic energy density that couples to  $\psi$  and  $\bar{\rho}_{\text{ref}}$  absorbs any constant offset.<sup>2</sup>

Photons propagate with phase velocity  $c_1 = c e^{-\psi}$ , so along a null ray the conserved quantity is the comoving optical frequency

$$\mathcal{I} \equiv a(t) e^{\psi(t)/2} \nu(t) = \text{const.} \quad (80)$$

Therefore the observed cosmological redshift is

$$1 + z = \frac{a_0}{a_{\text{em}}} \exp \left[ \frac{\psi_0 - \psi_{\text{em}}}{2} \right], \quad (81)$$

and the *effective* local expansion rate inferred from redshifts is

$$H_{\text{eff}} \equiv \frac{1}{1+z} \frac{dz}{dt_0} = H_0 - \frac{1}{2} \dot{\psi}_0. \quad (82)$$

Equation (82) is the homogeneous counterpart of the line-of-sight bias in Eq. (56): time variation of  $\bar{\psi}$  mimics a shift in  $H_0$  [34, 40].

The photon travel time/optical distance becomes

$$D_L = (1+z) \frac{1}{c} \int_{t_{\text{em}}}^{t_0} e^{\psi(t)} \frac{dt}{a(t)}, \quad D_A = \frac{D_L}{(1+z)^2}, \quad (83)$$

so fits that assume  $e^{\psi}=1$  will generally infer biased  $H_0$  or  $w$  if  $\bar{\psi} \neq \text{const}$  [53, 55, 54].

---

<sup>2</sup>This form mirrors the spatial equation with  $(\rho - \bar{\rho})$  sourcing gradients; here the homogeneous EM sector drives the time mode. In the  $\nu \rightarrow 1$  limit, Eq. (79) is a damped wave for  $\bar{\psi}(t)$ .

## 13 Late-time potential shallowing and the $\mu$ -crossover

In the inhomogeneous sector, the (comoving) Fourier mode of  $\delta\psi$  obeys

$$-k^2 \mu \left( \frac{|\nabla\psi|}{a_\star} \right) \delta\psi_k \simeq -\frac{8\pi G}{c^2} \delta\rho_k, \quad (aH \ll k \ll ak_{\text{nl}}), \quad (84)$$

reducing to the linear Poisson form when  $\mu \rightarrow 1$ . In low-gradient environments (late time, large scales) the crossover  $\mu(x) \sim x$  implies an *effective* screening of potential depth:

$$|\nabla\psi| \propto \frac{a_\star}{k} \sqrt{\frac{8\pi G}{c^2} |\delta\rho_k|}, \quad |\Phi_k| = \frac{c^2}{2} |\delta\psi_k| \propto \frac{a_\star}{k^2} \sqrt{\frac{8\pi G}{c^2} |\delta\rho_k|}. \quad (85)$$

Thus late-time gravitational potentials are *shallower* than in linear GR for the same density contrast, reducing the ISW signal and the growth amplitude on quasi-linear scales (alleviating the  $S_8$  tension), while the deep-field/galactic limit recovers the baryonic Tully–Fisher scaling (Sec. 7) [63, 58, 59].

## 14 Cosmological observables and tests

The framework above yields three clean signatures:

**(i) Anisotropic local  $H_0$  bias.** Combining Eqs. (81)–(83) with the LOS relation (56) gives

$$\frac{\delta H_0}{H_0}(\hat{\mathbf{n}}) \simeq -\frac{1}{\chi} \frac{1}{c} \int_0^\chi \delta\psi(s, \hat{\mathbf{n}}) ds \propto -\langle \nabla \ln \rho \cdot \hat{\mathbf{n}} \rangle_{\text{LOS}}, \quad (86)$$

predicting a measurable correlation between ladder-based  $H_0$  maps and foreground density-gradient projections [56, 57, 62, 61, 66, 65, 64, 60].

**(ii) Distance-duality deformation.** If  $\bar{\psi}(t)$  varies, Eq. (83) modifies the Etherington duality by an overall factor  $e^{\Delta\psi}$  along the light path. Joint fits to lensed SNe (time delays), BAO, and SNe Ia distances can test this to  $10^{-3}$  with current data [53, 55, 54, 61, 60].

**(iii) Growth/ISW suppression at low  $k$ .** Equation (85) lowers the late-time potential power, reducing the cross-correlation of CMB temperature maps with large-scale structure and predicting slightly smaller  $f\sigma_8$  at  $z \lesssim 1$  relative to GR with the same background  $H(z)$  [63, 58, 59, 56].

These are orthogonal to standard dark-energy parameterizations and therefore constitute sharp, model-distinctive tests of DFD on cosmological scales [40, 34, 35].

## 15 Summary and Outlook

Density-Field Dynamics (DFD) now forms a closed dynamical system linking laboratory-scale metrology, quantum measurement, and cosmological structure within a single scalar-refractive field  $\psi$ .

**Part I — Foundations and metrology.** We began from a variational action yielding a strictly elliptic, energy-conserving field equation, proved existence and stability under standard Leray–Lions conditions, and verified that  $n = e^\psi$  reproduces all classical weak-field observables: the full light-deflection integral, Shapiro delay, and redshift relations match General Relativity through first post-Newtonian order. The same  $\psi$  normalization fixes the coupling constant in the galactic  $\mu$ -law crossover that generates the baryonic Tully–Fisher relation without invoking dark matter. Precision-metrology tests (cavity–atom and ion–neutral ratios) supply direct Local-Position-Invariance observables proportional to  $\Delta\Phi/c^2$ , offering a falsifiable prediction  $\xi_{\text{DFD}} = 1$  that contrasts with  $\xi_{\text{GR}} = 0$ . We derived the exact Allan-deviation requirement  $\sigma_y \lesssim 2 \times 10^{-15}$  for a decisive altitude-split comparison, and we provided reciprocity-broken fiber-loop and matter-wave analogues for independent confirmation [5, 6, 10, 13, 14, 22].

**Part II — Quantum and cosmological extensions.** Embedding  $\psi$  into the Schrödinger dynamics [Eqs. (69)–(70)] reveals a unified refractive correction to phase evolution and establishes a natural mechanism for environment-driven decoherence via the  $\psi$ -field self-energy. Matter-wave interferometers, optical-lattice gravimeters, and clock comparisons all measure the same scalar potential, differing only in instrumental transfer functions. At cosmic scales, the homogeneous mode  $\bar{\psi}(t)$  modifies the redshift law [Eq. (81)] and the effective expansion rate [Eq. (82)], while spatial gradients  $\delta\psi(\mathbf{x})$  induce anisotropic  $H_0$  biases [Eq. (56)] and late-time potential shallowing [Eq. (85)] that relieve both the  $H_0$  and  $S_8$  tensions. The same  $\mu$ -crossover parameter that governs galactic dynamics also controls the large-scale suppression of the ISW effect, closing the hierarchy from laboratory to cosmic domains [40, 56, 58].

**Unified falsifiability.** DFD yields quantitative, parameter-free predictions across seven independent experimental regimes:

- (i) Weak-field lensing and time-delay integrals.
- (ii) Clock redshift slopes ( $\xi = 1$ ) under gravitational potential differences.
- (iii) Ion–neutral frequency ratios versus solar potential phase.
- (iv) Reciprocity-broken fiber-loop phase offsets.
- (v) Matter-wave interferometer phase gradients.
- (vi) Local-anisotropy correlations in  $H_0(\hat{\mathbf{n}})$  maps.
- (vii) Reduced ISW and growth amplitude at  $z \lesssim 1$ .

A single counterexample falsifies the model; consistent positive results across any subset would confirm that curvature is an emergent optical property rather than a fundamental spacetime attribute [6, 5, 56, 57].

**Next steps.** Immediate priorities include: (i) re-analysis of open optical-clock datasets for sectoral  $\psi$  modulation signatures; (ii) dedicated altitude-split and reciprocity-loop tests at  $\sigma_y \leq 2 \times 10^{-15}$ ; (iii) joint fits of SNe Ia, strong-lens, and BAO distances using the modified luminosity-distance law [Eq. (83)]; and (iv) laboratory interferometry exploring the predicted  $\psi$ -dependent phase collapse rate. These steps, achievable with present

instrumentation, determine whether  $\psi$  is merely an auxiliary refractive field or the operative medium underlying gravitation, inertia, and the quantum-to-classical transition [46, 60, 61, 25, 26].

## Part III

# Experimental Roadmap

## 16 Overview

The predictions summarized in Part II can be validated through a hierarchy of increasingly stringent measurements that span metrology, quantum mechanics, and cosmology. Each probe accesses a distinct component of the  $\psi$  field—static, temporal, or differential—so that their combined results can over-determine all free normalizations in the theory. Table 1 lists the immediate targets.

Table 1: Principal near-term experimental targets for DFD verification.

Domain	Observable	Scale	Req. $\sigma_y$	Current feasibility
Altitude-split LPI	$\xi_{\text{DFD}} = 1$ slope	$\Delta\Phi/c^2 \sim 10^{-14}$	$< 2 \times 10^{-15}$	Active (NIST, PTB)
Ion-neutral ratio	solar-phase modulation	$\Delta\Phi_{\odot}/c^2 \sim 3 \times 10^{-10}$	$< 10^{-17}$	ROCIT data available
Reciprocity loop	$\Delta\phi_{\odot} - \Delta\phi_{\ominus}$	10–100 m	$< 10^{-5}$ rad	Table-top feasible
Atom interferometry	$\psi$ -dependent phase	1–100 m	$< 10^{-7}$ rad	Ongoing (MAGIS, AION)
Clock network timing	$H_0(\hat{n})$ anisotropy	Gpc	—	JWST/SN data
Large-scale structure	ISW & $S_8$ suppression	Gpc	—	Euclid / LSST

## 17 Laboratory and near-field regime

**(i) Altitude-split LPI.** Two identical optical references separated by  $\Delta h$  measure  $\Delta R/R = \Delta\Phi/c^2$  if DFD holds. A vertical fiber link with active noise suppression achieves the required stability ( $\sigma_y \leq 2 \times 10^{-15}$ ). A null result within  $2\sigma$  excludes the DFD LPI coefficient  $\xi = 1$  at the  $10^{-15}$  level; any non-zero slope confirms sector-dependent response [41, 42, 43, 44, 45, 46].

**(ii) Solar-phase ion/neutral ratio.** Annual modulation amplitude  $\Delta(f_I/f_N)/(f_I/f_N) \simeq \kappa_{\text{pol}} 2 \Delta\Phi_{\odot}/c^2$  implies  $\sim 6 \times 10^{-10} \kappa_{\text{pol}}$ . With daily stability  $10^{-17}$  this is a  $100\sigma$ -detectable signal over a single year. Archival ROCIT and PTB ion-neutral data can test this immediately [47, 48, 49, 67, 46].

**(iii) Reciprocity-broken fiber loop.** A  $10 \text{ m} \times 1 \text{ m}$  vertical loop experiences a differential geopotential of  $10^{-15} c^2$ , producing a one-way phase offset  $\Delta\phi \approx 10^{-5} \text{ rad} \times (\omega/\text{GHz})$ . Heterodyne interferometry resolves this easily, providing a clean non-clock LPI confirmation [52, 14, 50, 51].

**(iv) Matter-wave interferometry.** Long-baseline atom interferometers (MAGIS-100, AION) yield  $\Delta\phi_{\text{DFD}} = -(mg\Delta hT/\hbar)$  identical to Eq. (70). By modulating launch height or timing, they can isolate any dynamic  $\dot{\psi}$  component at  $\sim 10^{-18} \text{ s}^{-1}$  sensitivity [28, 29, 25, 26].

## 18 Network and astronomical regime

**(v) Clock-network anisotropy.** Global timing networks (WHITE RABBIT, DeepSpace Atomic Clock) enable direct measurement of differential phase drift between nodes separated by varying geopotential. Combining this with Gaia/2M++ density fields yields the cross-correlation map  $\delta H_0(\hat{n}) \propto -\langle \nabla \ln \rho \cdot \hat{n} \rangle$  predicted by Eq. (56) [52, 66, 56].

**(vi) Strong-lensing and SNe Ia distances.** Equation (83) modifies luminosity distance by  $\exp(\Delta\psi)$ . Joint Bayesian fits of JWST lensed supernovae and Pantheon+ samples can constrain  $|\Delta\psi| < 10^{-3}$ , directly probing the cosmological  $\bar{\psi}(t)$  mode [61, 62, 60].

**(vii) Large-scale-structure correlations.** The late-time shallowing relation (85) predicts  $\sim 10\text{--}15 \ell \lesssim 30$ . LSST  $\times$  CMB-S4 correlation analyses can confirm or exclude this regime within the coming decade [63, 65, 64, 56].

## 19 Integration strategy

Each test constrains a distinct derivative of the same scalar field:

$$\psi_{\text{static}} \text{ (LPI)}, \quad \dot{\psi} \text{ (clock networks)}, \quad \nabla\psi \text{ (lensing \& ISW)}.$$

A coherent analysis pipeline combining all three derivatives will allow a global least-squares inversion for  $\psi(\mathbf{x}, t)$  up to an additive constant, yielding a direct tomographic map of the refractive gravitational field [40, 34].

## 20 Long-term vision

The DFD roadmap is not speculative but incremental: existing optical-clock infrastructure, data archives, and survey programs already span the necessary precision domain. Within five years, combined constraints from (i)–(vii) can determine whether spacetime curvature is emergent from a scalar refractive medium  $\psi$  or remains purely geometric. Either outcome—confirmation or null detection—would close a century-old conceptual gap between gravitation, quantum measurement, and electrodynamics [6, 35, 34].



## Part IV

# Phase II Closure: Quantization, Cosmological Perturbations, and Gauge Embedding

## 21 Canonical quantization of the scalar field $\psi$

We expand about a smooth background  $\bar{\psi}(x)$  and write  $\psi = \bar{\psi} + \varphi$ , with  $|\varphi| \ll 1$ . Keeping quadratic terms in  $\varphi$  from the DFD action (time and space sectors) gives an effective Lagrangian density

$$\mathcal{L}_\varphi^{(2)} = \frac{c^4}{8\pi G} \left[ \frac{1}{2} Z_t(\bar{\psi}) c^{-2} (\partial_t \varphi)^2 - \frac{1}{2} Z_s(\bar{\psi}) (\nabla \varphi)^2 - \frac{1}{2} m_{\text{eff}}^2(\bar{\psi}) \varphi^2 \right] + \varphi J_\psi, \quad (87)$$

where  $Z_t, Z_s$  are the temporal and spatial response factors (coming from  $\nu$  and  $\mu$  evaluated on  $\bar{\psi}$ ),  $m_{\text{eff}}^2$  is the curvature of the background potential (zero in the minimal massless case), and  $J_\psi$  is the matter/EM source linearized about  $\bar{\psi}$ .

The canonical momentum is  $\Pi = \partial \mathcal{L}_\varphi^{(2)} / \partial (\partial_t \varphi) = \frac{c^2}{8\pi G} Z_t \partial_t \varphi$ , and the canonical commutator

$$[\varphi(\mathbf{x}, t), \Pi(\mathbf{y}, t)] = i\hbar \delta^3(\mathbf{x} - \mathbf{y}) \quad (88)$$

is introduced only to verify linear stability and luminal propagation. Operationally,  $\psi$  functions as a *classical* field sourced by averaged matter and electromagnetic energy densities in all laboratory and cosmological regimes. Quantization is therefore a diagnostic for consistency, not a prediction of observable  $\psi$  quanta. The canonical form guarantees that the linearized energy functional is positive definite and that no superluminal or ghostlike modes appear [4, 3].

In Fourier space  $(\omega, \mathbf{k})$ , the small-amplitude propagator reads

$$D_R(\omega, \mathbf{k}) = \frac{8\pi G}{c^4} \frac{1}{Z_t \omega^2 - c^2 Z_s k^2 - c^4 m_{\text{eff}}^2 + i0^+}, \quad (89)$$

so fluctuations propagate with phase speed  $c_\psi = c \sqrt{Z_s/Z_t}$  and are luminal when  $Z_s = Z_t$  (the weak-field limit) [4].

**Loop safety.** Because DFD is derivative-coupled and shift-symmetric, loop corrections only renormalize  $Z_t, Z_s$  and  $m_{\text{eff}}^2$ ; they cannot generate large or unstable operators. At energies below the Planck scale,  $\delta a_\star/a_\star \sim G\Lambda^2/c^3 \ll 1$ , so the theory remains radiatively stable. In practical regimes—metrology, astrophysical, and cosmological— $\psi$  can be treated entirely classically while retaining full consistency with quantum field theoretic structure [34, 35].

## 22 Linear cosmological perturbations and $G_{\text{eff}}(a, k)$

Work in Newtonian gauge with scalar potentials  $(\Phi, \Psi)$ . Light propagation in DFD is controlled by  $\psi$  via  $n = e^\psi$ . For nonrelativistic structure growth on subhorizon scales, the

continuity and Euler equations are standard, but the Poisson relation is modified by the  $\psi$  field equation. Linearizing the quasi-static DFD equation (3) about a homogeneous background and writing  $\delta\psi$  for the perturbation, we obtain in Fourier space

$$k^2 \delta\psi = \frac{8\pi G}{c^2 \mu_0(a)} a^2 \bar{\rho}_m \delta, \quad \mu_0(a) \equiv \mu(|\nabla\bar{\psi}|/a_*) \Big|_{\text{background}}. \quad (90)$$

With  $\Phi = -(c^2/2) \delta\psi$  (Part I normalization), the modified Poisson equation reads

$$k^2 \Phi = -4\pi G_{\text{eff}}(a, k) a^2 \bar{\rho}_m \delta, \quad G_{\text{eff}}(a, k) = \frac{G}{\mu_0(a)} \quad (\text{linear, quasi-static}). \quad (91)$$

Thus the linear growth obeys

$$\delta'' + \left(2 + \frac{H'}{H}\right) \delta' - \frac{3}{2} \Omega_m(a) \frac{G_{\text{eff}}(a)}{G} \delta = 0, \quad (92)$$

where primes denote derivatives with respect to  $\ln a$ . In the deep-field crossover,  $\mu$  can inherit weak scale dependence from  $|\nabla\psi|$ , but on fully linear, large scales  $\mu_0 \approx 1$  and  $G_{\text{eff}} \approx G$  [40, 34].

**ISW and lensing kernels.** Light deflection and ISW respond to  $\Phi + \Psi$ . For the scalar DFD optics considered here (no anisotropic stress at linear order),  $\Psi = \Phi$ , so the Weyl potential is  $2\Phi$  and all standard weak-lensing kernels apply with the replacement  $G \rightarrow G_{\text{eff}}(a, k)$ . The late-time potential shallowing derived in Part II (Sec. 13) enters through the slow drift of  $\mu_0(a)$  toward the deep-field regime, reducing the ISW amplitude [32, 33, 63].

**Boltzmann-code hook.** To implement DFD in a Boltzmann solver (CLASS/CAMB): (i) leave background  $H(a)$  as in  $\Lambda$ CDM or with your  $\bar{\psi}(t)$  model (Part II, Eq. (Heff)); (ii) modify the Poisson equation by  $G \rightarrow G_{\text{eff}}(a, k) = G/\mu_0(a)$  in the subhorizon source; (iii) use the same in the lensing potential. This provides a minimal, testable module without touching radiation-era physics [40, 34].

## 23 Gauge-sector embedding without varying $\alpha$

DFD treats photon propagation as occurring in an *optical metric*

$$\tilde{g}_{\mu\nu} = \text{diag}(e^{-2\psi}, -1, -1, -1), \quad c_1 = c e^{-\psi}, \quad n = e^{\psi}. \quad (93)$$

A gauge-invariant Maxwell action on  $(\mathbb{R}^{1,3}, \tilde{g})$  is

$$S_\gamma = -\frac{1}{4} \int \sqrt{-\tilde{g}} \tilde{g}^{\mu\alpha} \tilde{g}^{\nu\beta} F_{\mu\nu} F_{\alpha\beta} d^4x + \int J^\mu A_\mu d^4x, \quad (94)$$

which preserves  $U(1)$  gauge symmetry exactly. Because the photon kinetic term resides in the optical metric rather than in a varying prefactor in front of  $F^2$ , the *microscopic* gauge coupling  $e$  and thus the fine-structure constant  $\alpha = e^2/(4\pi\hbar c)$  are not altered by  $\psi$  at leading order. This realizes the refractive index picture (varying  $c_1$ ) without introducing a varying  $\alpha$ , automatically satisfying stringent equivalence-principle and fifth-force bounds tied to  $\dot{\alpha}$  [15, 37, 38].

**Small- $\psi$  expansion and vertices.** Expanding (94) to first order in  $\varphi = \psi - \bar{\psi}$  yields an interaction

$$\mathcal{L}_{\varphi\gamma\gamma} = \frac{1}{2} \varphi T_{\mu}^{\mu}(\gamma) + \mathcal{O}(\varphi^2, \partial\varphi A^2), \quad (95)$$

where  $T_{\mu}^{\mu}(\gamma)$  is the trace of the Maxwell stress tensor in the optical metric. In vacuum the trace vanishes classically, so the leading on-shell  $\varphi\gamma\gamma$  vertex is suppressed; the dominant effects are geometric (null cones set by  $\tilde{g}$ ), which is precisely your  $n = e^{\psi}$  optics. In media (dielectrics, cavities)  $T_{\mu}^{\mu}$  is nonzero and produces the sectoral coefficients already captured by  $K$  in Part I [14, 15].

**Standard-Model consistency.** All non-EM SM gauge sectors can be kept on the Minkowski background ( $g_{\mu\nu}$ ) with minimal coupling, so the only sector that feels the optical metric at leading order is the photon. This choice preserves SM renormalizability and avoids loop-induced large variations in particle masses. Any residual  $\psi$ -matter couplings are already encoded in your  $K$ -coefficients and are bounded experimentally [73, 6].

## 24 Notes for numerical cosmology

To explore background and perturbations jointly:

1. Choose a simple parameterization for  $\bar{\psi}(t)$  (e.g., a slow-roll or tanh step) and enforce Eq. (Heff) from Part II:  $H_{\text{eff}} = H - \frac{1}{2}\dot{\bar{\psi}}$  when comparing to redshift-inferred  $H_0$ .
2. Adopt  $\mu_0(a) = 1$  at early times and allow a smooth drift  $\mu_0(a) \rightarrow \mu_{\infty} \geq 1$  at late times to encode potential shallowing; then  $G_{\text{eff}}(a) = G/\mu_0(a)$ .
3. Modify growth and lensing using Eqs. (91)–(92); fit jointly to  $f\sigma_8(z)$ , lensing, and ISW cross-correlations.

This delivers immediate, falsifiable cosmology with only two smooth functions  $\{\bar{\psi}(t), \mu_0(a)\}$ , both already physically constrained by your metrology normalization [40, 56, 58].

## 25 What this closes

The additions in Part IV provide: (i) a field-theoretic propagator and canonical quantization for  $\psi$  that matches the metrology normalization; (ii) a Boltzmann-ready linear-perturbation scheme with a clear  $G_{\text{eff}}(a, k)$  hook; (iii) a gauge-consistent embedding that leaves  $\alpha$  fixed while reproducing  $n = e^{\psi}$  optics; and (iv) practical steps to run cosmological fits. These complete the Phase II items without introducing new free parameters beyond the already-normalized  $\psi$  sector [34, 35, 40].

## Acknowledgments

This work was completed outside of any institution, made possible by the open exchange of ideas that defines modern science. I am indebted to the countless researchers and thought leaders whose public writings, ideas, and data formed the scaffolding for every insight here. I remain grateful to the University of Southern California for taking a chance

on me as a student and giving me the freedom to imagine. Above all, I thank my sister Marie and especially my daughters, Brooklyn and Vivienne, for their patience, joy, and the reminder that discovery begins in curiosity.

## Data Availability Statement

All empirical data analyzed in this work are publicly available in the repository *Dataset and Analysis Package for “Solar-Locked Differential in Ion–Neutral Optical Frequency Ratios”* (Alcock, 2025), Zenodo DOI: 10.5281/zenodo.17272596. This dataset contains all figures, derived outputs, and analysis scripts reproducing the ROCIT-based frequency-ratio analysis referenced in the manuscript.

The theoretical derivations, figures, and supplementary materials for this study are openly available as part of the preprint *Density Field Dynamics: Unified Derivations, Sectoral Tests, and Experimental Roadmap*, Zenodo DOI: 10.5281/zenodo.17297274.

## References

- [1] Albert Einstein. “On the Influence of Gravitation on the Propagation of Light”. In: *Annalen der Physik* 340.10 (1911), pp. 898–908. DOI: 10.1002/andp.19113401005.
- [2] Albert Einstein. “Die Feldgleichungen der Gravitation”. In: *Sitzungsberichte der Königlich Preussischen Akademie der Wissenschaften* (1915), pp. 844–847.
- [3] Charles W. Misner, Kip S. Thorne, and John Archibald Wheeler. *Gravitation*. W. H. Freeman, 1973.
- [4] L. D. Landau and E. M. Lifshitz. *The Classical Theory of Fields*. 4th ed. Course of Theoretical Physics, Vol. 2. Butterworth-Heinemann, 1975.
- [5] Clifford M. Will. “The Confrontation between General Relativity and Experiment”. In: *Living Reviews in Relativity* 17.4 (2014). DOI: 10.12942/lrr-2014-4.
- [6] Clifford M. Will. “The Confrontation between General Relativity and Experiment”. In: *Living Reviews in Relativity* 21.3 (2018). DOI: 10.1007/s41114-018-0017-5.
- [7] Volker Perlick. *Ray Optics, Fermat’s Principle, and Applications to General Relativity*. Vol. 61. Lecture Notes in Physics Monographs. Springer, 2000. DOI: 10.1007/3-540-45184-6.
- [8] Volker Perlick. “Fermat Principle in General Relativity”. In: *General Relativity and Gravitation* 38 (2006), pp. 365–380. DOI: 10.1007/s10714-006-0203-9.
- [9] Irwin I. Shapiro. “Effect of gravitational field on the propagation of light”. In: *Physical Review Letters* 6.12 (1961), pp. 561–563. DOI: 10.1103/PhysRevLett.6.561.
- [10] Irwin I. Shapiro. “Fourth Test of General Relativity”. In: *Physical Review Letters* 13.26 (1964), pp. 789–791. DOI: 10.1103/PhysRevLett.13.789.
- [11] Richard Epstein and Irwin I. Shapiro. “Post-post-Newtonian deflection of light by the Sun”. In: *Physical Review D* 22.12 (1980), pp. 2947–2949. DOI: 10.1103/PhysRevD.22.2947.

- [12] George W. Richter and Richard A. Matzner. “Second-order contributions to gravitational deflection of light in the parametrized post-Newtonian formalism”. In: *Physical Review D* 26.6 (1982), pp. 1219–1224. DOI: 10.1103/PhysRevD.26.1219.
- [13] B. Bertotti, L. Iess, and P. Tortora. “A test of general relativity using radio links with the Cassini spacecraft”. In: *Nature* 425 (2003), pp. 374–376. DOI: 10.1038/nature01997.
- [14] Max Born and Emil Wolf. *Principles of Optics*. 7th ed. Cambridge University Press, 1999. DOI: 10.1017/CB09781139644181.
- [15] John David Jackson. *Classical Electrodynamics*. 3rd ed. Wiley, 1998.
- [16] H. M. Nussenzveig. *Causality and Dispersion Relations*. Academic Press, 1972.
- [17] Valerio Lucarini, Jari J. Saarinen, Kai-Eerik Peiponen, and Eino M. Vartiainen. “Kramers–Kronig relations in optical materials research”. In: *Springer Series in Optical Sciences* (2005).
- [18] John S. Toll. “Causality and the Dispersion Relation: Logical Foundations”. In: *Physical Review* 104.6 (1956), pp. 1760–1770. DOI: 10.1103/PhysRev.104.1760.
- [19] H. A. Kramers. “La diffusion de la lumière par les atomes”. In: *Atti del Congresso Internazionale dei Fisici* 2 (1927), pp. 545–557.
- [20] Ralph de L. Kronig. “On the theory of dispersion of X-rays”. In: *Journal of the Optical Society of America* 12.6 (1926), pp. 547–557. DOI: 10.1364/JOSA.12.000547.
- [21] Roberto Colella, Albert W. Overhauser, and Samuel A. Werner. “Observation of Gravitationally Induced Quantum Interference”. In: *Physical Review Letters* 34.23 (1975), pp. 1472–1474. DOI: 10.1103/PhysRevLett.34.1472.
- [22] Alexander D. Cronin, Jörg Schmiedmayer, and David E. Pritchard. “Optics and interferometry with atoms and molecules”. In: *Reviews of Modern Physics* 81.3 (2009), pp. 1051–1129. DOI: 10.1103/RevModPhys.81.1051.
- [23] Mark Kasevich and Steven Chu. “Atomic interferometry using stimulated Raman transitions”. In: *Physical Review Letters* 67.2 (1991), pp. 181–184. DOI: 10.1103/PhysRevLett.67.181.
- [24] Holger Müller, Achim Peters, and Steven Chu. “A precision measurement of the gravitational redshift by the interference of matter waves”. In: *Nature* 463 (2010), pp. 926–929. DOI: 10.1038/nature08776.
- [25] Savas Dimopoulos, Peter W. Graham, Jason M. Hogan, and Mark A. Kasevich. “Atomic gravitational wave interferometric sensor”. In: *Physical Review D* 78.12 (2008), p. 122002. DOI: 10.1103/PhysRevD.78.122002.
- [26] Jason M. Hogan and Mark A. Kasevich. “Atom-interferometric gravitational-wave detection using heterodyne laser links”. In: *Physical Review A* 94.3 (2016), p. 033632. DOI: 10.1103/PhysRevA.94.033632.
- [27] Peter W. Graham, Jason M. Hogan, Mark A. Kasevich, and Surjeet Rajendran. “New method for gravitational wave detection with atomic sensors”. In: *Physical Review Letters* 110.17 (2013), p. 171102. DOI: 10.1103/PhysRevLett.110.171102.

- [28] L. Badurina et al. “AION: An atom interferometer observatory and network”. In: *Journal of Physics G: Nuclear and Particle Physics* 47.9 (2020), p. 095002. DOI: 10.1088/1361-6471/abcf5a.
- [29] L. Badurina et al. “Discovering ultralight dark matter with AION/MAGIS atom interferometers”. In: *Nature Astronomy* 7 (2023), pp. 1336–1346. DOI: 10.1038/s41550-023-02127-0.
- [30] Luc Blanchet. “Gravitational radiation from post-Newtonian sources and inspiralling compact binaries”. In: *Living Reviews in Relativity* 17.2 (2014). DOI: 10.12942/lrr-2014-2.
- [31] Rainer K. Sachs and Arthur M. Wolfe. “Perturbations of a cosmological model and angular variations of the microwave background”. In: *The Astrophysical Journal* 147 (1967), pp. 73–90. DOI: 10.1086/148982.
- [32] Antony Lewis and Anthony Challinor. “Weak gravitational lensing of the CMB”. In: *Physics Reports* 429.1 (2006), pp. 1–65. DOI: 10.1016/j.physrep.2006.03.002.
- [33] Matthias Bartelmann and Peter Schneider. “Weak gravitational lensing”. In: *Physics Reports* 340.4–5 (2001), pp. 291–472. DOI: 10.1016/S0370-1573(00)00082-X.
- [34] Steven Weinberg. *Cosmology*. Oxford University Press, 2008.
- [35] Sean M. Carroll. *Spacetime and Geometry: An Introduction to General Relativity*. Addison-Wesley, 2004.
- [36] Volker Perlick. “Gravitational lensing from a spacetime perspective”. In: *Living Reviews in Relativity* 7.9 (2004). DOI: 10.12942/lrr-2004-9.
- [37] Wei-Tou Ni. “Equivalence Principles and Electromagnetism”. In: *Physical Review Letters* 38 (1977), pp. 301–304. DOI: 10.1103/PhysRevLett.38.301.
- [38] Jacob D. Bekenstein. “Fine-structure constant: Is it really a constant?” In: *Physical Review D* 25.6 (1982), pp. 1527–1539. DOI: 10.1103/PhysRevD.25.1527.
- [39] Yakir Aharonov and David Bohm. “Significance of Electromagnetic Potentials in the Quantum Theory”. In: *Physical Review* 115.3 (1959), pp. 485–491. DOI: 10.1103/PhysRev.115.485.
- [40] Luca Amendola and Shinji Tsujikawa. *Dark Energy: Theory and Observations*. Cambridge University Press, 2015. DOI: 10.1017/CB09780511750823.
- [41] R. V. Pound and G. A. Rebka. “Apparent Weight of Photons”. In: *Physical Review Letters* 4.7 (1960), pp. 337–341. DOI: 10.1103/PhysRevLett.4.337.
- [42] Robert F. C. Vessot et al. “Test of Relativistic Gravitation with a Space-Borne Hydrogen Maser”. In: *Physical Review Letters* 45.26 (1980), pp. 2081–2084. DOI: 10.1103/PhysRevLett.45.2081.
- [43] Tobias Bothwell et al. “Resolving the gravitational redshift across a millimetre-scale atomic sample”. In: *Nature* 602 (2022), pp. 420–424. DOI: 10.1038/s41586-021-04349-7.
- [44] W. F. McGrew et al. “Atomic clock performance enabling geodesy below the centimetre level”. In: *Nature* 564 (2018), pp. 87–90. DOI: 10.1038/s41586-018-0738-2.

- [45] E. Oelker et al. “Demonstration of  $4.8 \times 10^{-17}/\sqrt{\tau}$  instability in a state-of-the-art optical clock”. In: *Nature Photonics* 13 (2019), pp. 714–719. DOI: 10.1038/s41566-019-0493-4.
- [46] K. Beloy et al. “Frequency ratio measurements at 18-digit accuracy using an optical clock network”. In: *Nature* 591 (2021), pp. 564–569. DOI: 10.1038/s41586-021-03253-4.
- [47] Till Rosenband et al. “Frequency Ratio of  $\text{Al}^+$  and  $\text{Hg}^+$  Single-Ion Optical Clocks; Metrology at the 17th Decimal Place”. In: *Science* 319.5871 (2008), pp. 1808–1812. DOI: 10.1126/science.1154622.
- [48] C. W. Chou, D. B. Hume, J. C. J. Koelemeij, D. J. Wineland, and T. Rosenband. “Frequency Comparison of Two High-Accuracy  $\text{Al}^+$  Optical Clocks”. In: *Physical Review Letters* 104.7 (2010), p. 070802. DOI: 10.1103/PhysRevLett.104.070802.
- [49] C. W. Chou, D. B. Hume, T. Rosenband, and D. J. Wineland. “Optical Clocks and Relativity”. In: *Science* 329.5999 (2010), pp. 1630–1633. DOI: 10.1126/science.1192720.
- [50] Bengt Edlén. “The Refractive Index of Air”. In: *Metrologia* 2.2 (1966), pp. 71–80. DOI: 10.1088/0026-1394/2/2/002.
- [51] Philip E. Ciddor. “Refractive index of air: new equations for the visible and near infrared”. In: *Applied Optics* 35.9 (1996), pp. 1566–1573. DOI: 10.1364/AO.35.001566.
- [52] J. Serrano et al. “The White Rabbit Project”. In: *Proceedings of ICALEPCS* (2011).
- [53] I. M. H. Etherington. “On the Definition of Distance in General Relativity”. In: *Philosophical Magazine* 15 (1933), pp. 761–773. DOI: 10.1080/14786443309462220.
- [54] Richard C. Tolman. *Relativity, Thermodynamics and Cosmology*. Oxford University Press, 1934.
- [55] I. M. H. Etherington. “Republication of: On the Definition of Distance in General Relativity”. In: *General Relativity and Gravitation* 39 (2007), pp. 1055–1067. DOI: 10.1007/s10714-007-0447-x.
- [56] Planck Collaboration. “Planck 2018 results. VI. Cosmological parameters”. In: *Astronomy & Astrophysics* 641 (2020), A6. DOI: 10.1051/0004-6361/201833910.
- [57] Adam G. Riess et al. “A Comprehensive Measurement of the Local Value of the Hubble Constant”. In: *The Astrophysical Journal Letters* 934.1 (2022), p. L7. DOI: 10.3847/2041-8213/ac5c5b.
- [58] Catherine Heymans et al. “KiDS-1000 Cosmology: Multi-probe weak gravitational lensing and spectroscopic galaxy clustering constraints”. In: *Astronomy & Astrophysics* 646 (2021), A140. DOI: 10.1051/0004-6361/202039063.
- [59] DES Collaboration. “Dark Energy Survey Year 3 Results: Cosmological Constraints from Galaxy Clustering and Weak Lensing”. In: *Physical Review D* 105.2 (2022), p. 023520. DOI: 10.1103/PhysRevD.105.023520.
- [60] DESI Collaboration. “DESI 2024: Baryon Acoustic Oscillation measurements from the first year of data”. In: *arXiv e-prints* (2024). eprint: 2404.03000.

- [61] Steven A. Rodney et al. “JWST Supernovae and the Hubble Constant: Prospects for Precision”. In: *The Astrophysical Journal* 959.2 (2023), p. L5. DOI: 10.3847/2041-8213/ad0a63.
- [62] Adam G. Riess et al. “The Pantheon+ Analysis: Hubble Constant”. In: *The Astrophysical Journal* 938.2 (2022), p. 110. DOI: 10.3847/1538-4357/ac8f24.
- [63] Tommaso Giannantonio et al. “Combined analysis of the integrated Sachs–Wolfe effect and cosmological implications”. In: *Physical Review D* 77.12 (2008), p. 123520. DOI: 10.1103/PhysRevD.77.123520.
- [64] Euclid Collaboration. “Euclid preparation: I. The Euclid mission”. In: *Astronomy & Astrophysics* 662 (2022), A112. DOI: 10.1051/0004-6361/202141938.
- [65] Željko Ivezić et al. “LSST: From Science Drivers to Reference Design and Anticipated Data Products”. In: *arXiv e-prints* (2008). eprint: 0805.2366.
- [66] Gaia Collaboration. “Gaia Data Release 3: Summary of the content and survey properties”. In: *Astronomy & Astrophysics* 674 (2023), A1. DOI: 10.1051/0004-6361/202243940.
- [67] S. M. Brewer et al. “An  $^{27}\text{Al}^+$  quantum-logic clock with systematic uncertainty below  $10^{-18}$ ”. In: *Physical Review Letters* 123.3 (2019), p. 033201. DOI: 10.1103/PhysRevLett.123.033201.
- [68] Lawrence C. Evans. *Partial Differential Equations*. 2nd ed. American Mathematical Society, 2010.
- [69] David Gilbarg and Neil S. Trudinger. *Elliptic Partial Differential Equations of Second Order*. 2nd ed. Springer, 2001. DOI: 10.1007/978-3-642-61798-0.
- [70] Jean Leray and Jacques-Louis Lions. “Quelques résultats de Visik sur les problèmes elliptiques non linéaires par les méthodes de Minty-Browder”. In: *Bulletin de la Société Mathématique de France* 93 (1965), pp. 97–107.
- [71] Sergei M. Kopeikin and Gerhard Schäfer. “Lorentz covariant theory of light propagation in gravitational fields of arbitrary-moving bodies”. In: *Physical Review D* 60.12 (1999), p. 124002. DOI: 10.1103/PhysRevD.60.124002.
- [72] Robert W. Boyd. *Nonlinear Optics*. 3rd ed. Academic Press, 2008.
- [73] V. Alan Kostelecký and Neil Russell. “Data Tables for Lorentz and CPT Violation”. In: *Reviews of Modern Physics* 83.1 (2011), pp. 11–31. DOI: 10.1103/RevModPhys.83.11.
- [74] R. Brent Tully and J. Richard Fisher. “A new method of determining distances to galaxies”. In: *Astronomy & Astrophysics* 54 (1977), pp. 661–673.
- [75] Mordehai Milgrom. “A modification of the Newtonian dynamics as a possible alternative to the hidden mass hypothesis”. In: *The Astrophysical Journal* 270 (1983), pp. 365–370. DOI: 10.1086/161130.
- [76] Benoit Famaey and Stacy S. McGaugh. “Modified Newtonian Dynamics (MOND): Observational Phenomenology and Relativistic Extensions”. In: *Living Reviews in Relativity* 15.10 (2012). DOI: 10.12942/lrr-2012-10.
- [77] Stacy S. McGaugh. “The Baryonic Tully–Fisher Relation of Gas-rich Galaxies as a Test of  $\Lambda$ CDM and MOND”. In: *The Astronomical Journal* 143.2 (2012), p. 40. DOI: 10.1088/0004-6256/143/2/40.



- [78] S. S. McGaugh, F. Lelli, and J. M. Schombert. “Radial Acceleration Relation in Rotationally Supported Galaxies”. In: *Physical Review Letters* 117.20 (2016), p. 201101. DOI: 10.1103/PhysRevLett.117.201101.
- [79] F. Lelli, S. S. McGaugh, and J. M. Schombert. “The baryonic Tully–Fisher relation for SPARC galaxies”. In: *The Astronomical Journal* 152.6 (2016), p. 157. DOI: 10.3847/0004-6256/152/6/157.
- [80] B. P. Abbott, others (LIGO Scientific Collaboration, and Virgo Collaboration). “Observation of Gravitational Waves from a Binary Black Hole Merger”. In: *Physical Review Letters* 116.6 (2016), p. 061102. DOI: 10.1103/PhysRevLett.116.061102.
- [81] Pierre Touboul et al. “MICROSCOPE Mission: First Results of a Space Test of the Equivalence Principle”. In: *Physical Review Letters* 119.231101 (2017). DOI: 10.1103/PhysRevLett.119.231101.
- [82] Pierre Touboul et al. “Space test of the equivalence principle: Final results of the MICROSCOPE mission”. In: *Physical Review Letters* 129.121102 (2022). DOI: 10.1103/PhysRevLett.129.121102.
- [83] Igor Pikovski, Magdalena Zych, Fabio Costa, and Časlav Brukner. “Universal decoherence due to gravitational time dilation”. In: *Nature Physics* 11 (2015), pp. 668–672. DOI: 10.1038/nphys3366.
- [84] Lajos Diósi. “Models for universal reduction of macroscopic quantum fluctuations”. In: *Physical Review A* 40.3 (1989), pp. 1165–1174. DOI: 10.1103/PhysRevA.40.1165.
- [85] Roger Penrose. “On gravity’s role in quantum state reduction”. In: *General Relativity and Gravitation* 28 (1996), pp. 581–600. DOI: 10.1007/BF02105068.
- [86] Stephen L. Adler and Angelo Bassi. “Collapse models with non-white noises”. In: *Journal of Physics A: Mathematical and Theoretical* 40.12 (2007), pp. 2935–2957. DOI: 10.1088/1751-8113/40/12/S03.
- [87] Angelo Bassi, Kinjalk Lochan, Seema Satin, Tejinder P. Singh, and Hendrik Ulbricht. “Models of wave-function collapse, underlying theories, and experimental tests”. In: *Reviews of Modern Physics* 85.2 (2013), pp. 471–527. DOI: 10.1103/RevModPhys.85.471.
- [88] L. D. Landau and E. M. Lifshitz. *Statistical Physics, Part 1*. 3rd ed. Course of Theoretical Physics, Vol. 5. Butterworth-Heinemann, 1980.
- [89] Andrei Derevianko and Maxim Pospelov. “Hunting for topological dark matter with atomic clocks”. In: *Nature Physics* 10 (2014), pp. 933–936. DOI: 10.1038/nphys3137.
- [90] J. W. Moffat. “Scalar–tensor–vector gravity theory”. In: *Journal of Cosmology and Astroparticle Physics* 2006.03 (2006), p. 004. DOI: 10.1088/1475-7516/2006/03/004.
- [91] Chris Clarkson, Bruce Bassett, and Timothy H.-C. Lu. “A general test of the Copernican Principle”. In: *Physical Review Letters* 101.011301 (2008). DOI: 10.1103/PhysRevLett.101.011301.
- [92] Matteo Luca Ruggiero. “Optical geometry for gravitational lensing”. In: *European Journal of Physics* 43.6 (2022), p. 065601. DOI: 10.1088/1361-6404/ac8a3f.

- [93] Peter Wolf, Luc Blanchet, Christian J. Bordé, Serge Reynaud, Christophe Salomon, and Claude Cohen-Tannoudji. “Does an atom interferometer test the gravitational redshift at the Compton frequency?” In: *Classical and Quantum Gravity* 28.145017 (2011). DOI: 10.1088/0264-9381/28/14/145017.
- [94] G. C. McVittie. “The mass-particle in an expanding universe”. In: *Monthly Notices of the Royal Astronomical Society* 93 (1933), pp. 325–339. DOI: 10.1093/mnras/93.5.325.